



UNIVERSITY OF LEEDS

This is a repository copy of *The role of strain hardening in the transition from dislocation-mediated to frictional deformation of marbles within the Karakoram Fault Zone, NW India.*

White Rose Research Online URL for this paper:
<http://eprints.whiterose.ac.uk/124397/>

Version: Accepted Version

Article:

Wallis, D, Lloyd, GE orcid.org/0000-0002-7859-2486 and Hansen, LN (2018) The role of strain hardening in the transition from dislocation-mediated to frictional deformation of marbles within the Karakoram Fault Zone, NW India. *Journal of Structural Geology*, 107. pp. 25-37. ISSN 0191-8141

<https://doi.org/10.1016/j.jsg.2017.11.008>

© 2017 Elsevier Ltd. This manuscript version is made available under the CC-BY-NC-ND 4.0 license <http://creativecommons.org/licenses/by-nc-nd/4.0/>

Reuse

This article is distributed under the terms of the Creative Commons Attribution-NonCommercial-NoDerivs (CC BY-NC-ND) licence. This licence only allows you to download this work and share it with others as long as you credit the authors, but you can't change the article in any way or use it commercially. More information and the full terms of the licence here: <https://creativecommons.org/licenses/>

Takedown

If you consider content in White Rose Research Online to be in breach of UK law, please notify us by emailing eprints@whiterose.ac.uk including the URL of the record and the reason for the withdrawal request.

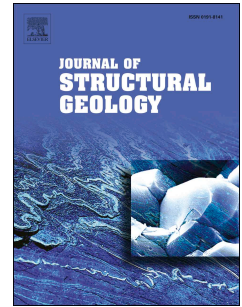


eprints@whiterose.ac.uk
<https://eprints.whiterose.ac.uk/>

Accepted Manuscript

The role of strain hardening in the transition from dislocation-mediated to frictional deformation of marbles within the Karakoram Fault Zone, NW India

David Wallis, Geoffrey E. Lloyd, Lars N. Hansen



PII: S0191-8141(17)30257-2

DOI: [10.1016/j.jsg.2017.11.008](https://doi.org/10.1016/j.jsg.2017.11.008)

Reference: SG 3555

To appear in: *Journal of Structural Geology*

Received Date: 5 June 2017

Revised Date: 11 October 2017

Accepted Date: 15 November 2017

Please cite this article as: Wallis, D., Lloyd, G.E., Hansen, L.N., The role of strain hardening in the transition from dislocation-mediated to frictional deformation of marbles within the Karakoram Fault Zone, NW India, *Journal of Structural Geology* (2017), doi: 10.1016/j.jsg.2017.11.008.

This is a PDF file of an unedited manuscript that has been accepted for publication. As a service to our customers we are providing this early version of the manuscript. The manuscript will undergo copyediting, typesetting, and review of the resulting proof before it is published in its final form. Please note that during the production process errors may be discovered which could affect the content, and all legal disclaimers that apply to the journal pertain.

1 **The role of strain hardening in the transition from dislocation-mediated to frictional**
2 **deformation of marbles within the Karakoram Fault Zone, NW India**

3 David Wallis^{1*}, Geoffrey E. Lloyd² and Lars N. Hansen¹

4 ¹*Department of Earth Sciences, University of Oxford, Oxford, UK, OX1 3AN,*

5 *David.Wallis@earth.ox.ac.uk*

6 ²*School of Earth and Environment, University of Leeds, Leeds, UK, LS2 9JT.*

7 **Corresponding author*

8 **Keywords**

9 Calcite; Schmid factor; resolved shear stress; strain hardening; seismogenesis; Karakoram
10 Fault Zone

11 **Abstract**

12 The onset of frictional failure and potentially seismogenic deformation in carbonate
13 rocks undergoing exhumation within fault zones depends on hardening processes that reduce
14 the efficiency of aseismic dislocation-mediated deformation as temperature decreases.
15 However, few techniques are available for quantitative analysis of dislocation slip system
16 activity and hardening in natural tectonites. Electron backscatter diffraction maps of crystal
17 orientations offer one such approach *via* determination of Schmid factors, if the palaeostress
18 conditions can be inferred and the critical resolved shear stresses of slip systems are
19 constrained. We analyse calcite marbles deformed in simple shear within the Karakoram
20 Fault Zone, NW India, to quantify changes in slip system activity as the rocks cooled during
21 exhumation. Microstructural evidence demonstrates that between ~300°C and 200–250°C the
22 dominant deformation mechanisms transitioned from dislocation-mediated flow to twinning

23 and frictional failure. However, Schmid factor analysis, considering critical resolved shear
24 stresses for yield of undeformed single crystals, indicates that the fraction of grains with
25 sufficient resolved shear stress for glide apparently increased with decreasing temperature.
26 Misorientation analysis and previous experimental data indicate that strain-dependent work
27 hardening is responsible for this apparent inconsistency and promoted the transition from
28 dislocation-mediated flow to frictional, and potentially seismogenic, deformation.

29 **1. Introduction**

30 Calcite exhibits marked velocity-weakening behaviour, which may promote
31 nucleation of unstable earthquake ruptures (Han *et al.*, 2010; Verberne *et al.*, 2015; Cowie *et*
32 *al.*, 2017). Faults hosted in calcite-rich lithologies are therefore major sources of seismic
33 hazard in zones of active continental deformation (Smith *et al.*, 2011). The depth extent of
34 earthquake nucleation in such faults broadly corresponds to the depth at which the activity of
35 temperature-dependent aseismic creep processes can prevent unstable frictional failure under
36 interseismic strain rate conditions (Scholz, 1988; Verberne *et al.*, 2015). Dislocation-
37 mediated deformation mechanisms (potentially including contributions from dislocation
38 creep, low-temperature plasticity, and/or dislocation-accommodated grain boundary sliding)
39 are commonly inferred to have operated in calcite-rich shear zones exhumed from mid-crustal
40 depths and in which the grain size and/or conditions were unfavourable for efficient diffusion
41 creep (e.g. Bestmann *et al.*, 2006; Rutter *et al.*, 2007; Wallis *et al.*, 2013; Parsons *et al.*,
42 2016). Therefore, competition between dislocation-mediated flow and frictional failure may
43 exert an important control on the depth limit of earthquake nucleation. However, the precise
44 microphysical processes that control this transition in natural fault zones remain poorly
45 constrained, particularly in situations where rocks are progressively exhumed during
46 deformation, resulting in a transition from aseismic flow to potentially seismogenic frictional

47 failure within the exhuming rock mass (Handy *et al.*, 2007). The strength of rocks undergoing
48 dislocation-mediated deformation is a function of the stresses required to activate dislocation
49 glide on particular crystallographic slip systems, which may depend on both environmental
50 conditions (e.g. temperature, pressure, and strain rate) and other state variables (e.g.
51 composition, dislocation density and distribution) (e.g., Hobbs *et al.*, 1972; de Bresser and
52 Spiers, 1997). However, it is challenging to determine the strength and activity of slip
53 systems during dislocation-mediated deformation in natural tectonites, and relatively few
54 techniques are available to do so. As a result, the precise controls on the transition from
55 aseismic creep to frictional failure and potentially seismogenic behaviour in natural fault
56 zones remain poorly constrained.

57 The most common approach to assess the relative activity of different slip systems in
58 natural tectonites is to interpret the slip system(s) most likely to have generated an observed
59 crystallographic preferred orientation (CPO); for example, by determining the slip system
60 inferred to have most readily rotated into orientations with high resolved shear stress (e.g.,
61 Toy *et al.*, 2008). However, such analysis is often limited to qualitative interpretations and
62 comparisons. More quantitative information can be gleaned by comparing natural and
63 experimental CPOs to results from simulations of polycrystal plasticity (e.g. Wenk *et al.*,
64 1987). However, this approach tends to place relatively loose constraints on slip system
65 activity due to the large parameter space that needs to be searched (i.e., typically many
66 combinations of slip system strengths and deformation geometries have to be tested) and
67 challenges in comparing natural and simulated CPO geometries quantitatively.

68 Another approach is to analyse crystallographic misorientations resulting from the
69 presence of dislocations within grains (Lloyd *et al.*, 1997; Bestmann and Prior, 2003;
70 Wheeler *et al.*, 2009). However, due to the limited angular resolution of commonly available

71 measurement techniques (e.g. $\sim 0.2^\circ$ for misorientation angles from conventional electron
72 backscatter diffraction, EBSD) such analysis can only sample the fraction of the dislocation
73 population that is arranged into relatively high misorientation substructures such as subgrain
74 boundaries (Prior, 1999). As such, ‘free’ dislocations that are not in subgrain boundaries can
75 be difficult to detect and generally require higher precision and more computationally
76 expensive techniques such as high-angular resolution electron backscatter diffraction (Wallis
77 *et al.*, 2016a, 2017). Moreover, it is unclear to what extent the measured dislocation content
78 was glissile or sessile during deformation. This ambiguity also often applies to direct
79 observation of dislocations, by transmission-electron imaging, chemical etching, or
80 decoration by oxidation.

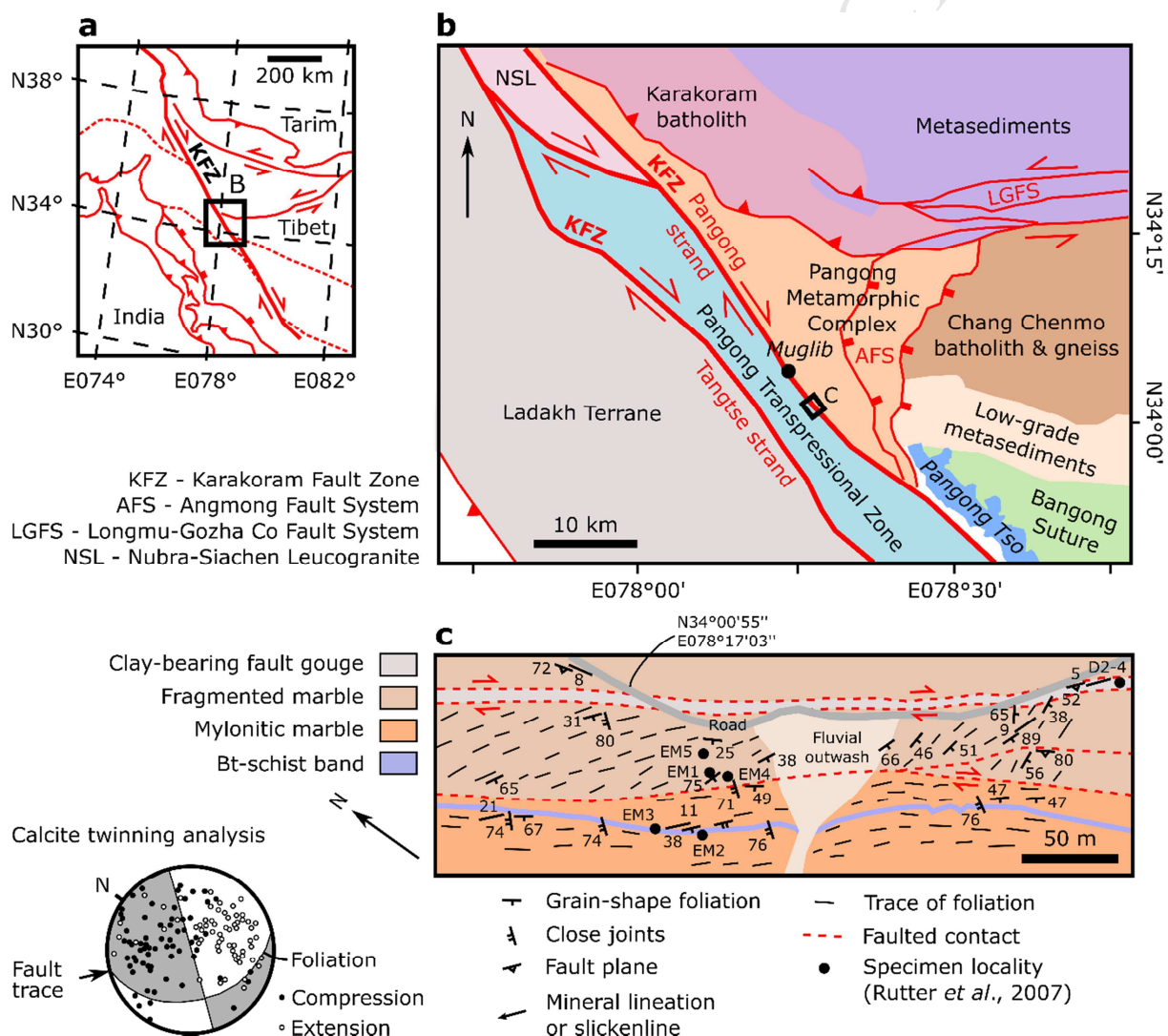
81 In this contribution, we exploit advances in EBSD (Prior *et al.*, 1999, 2009;
82 Bachmann *et al.*, 2010; Mainprice *et al.*, 2011) to develop a method of slip system analysis
83 based on determination of Schmid factors (Schmid, 1928; Schmid and Boas, 1950; Farla *et*
84 *al.*, 2011; Hansen *et al.*, 2011). The Schmid factor of a slip system quantitatively describes
85 the relation between resolved shear stress and applied stress state (the higher the Schmid
86 factor, the greater the resolved shear stress on the slip system). This orientation relationship is
87 typically qualitatively inferred when interpreting slip systems that contribute to CPO
88 development (e.g. Toy *et al.*, 2008). However, the Schmid factor not only quantifies this
89 relationship, but also allows for calculation of resolved shear stresses on each slip system,
90 and enables mapping of grains that are (un)favourably oriented for dislocation glide.
91 Relatively few geological studies have utilised detailed Schmid factor analysis. Most of these
92 focussed on stress states associated with radially-symmetric shortening or extension (e.g.
93 Ralser *et al.*, 1991; Farla *et al.*, 2011; Hansen *et al.*, 2011), and to our knowledge, only two
94 have considered simple shear, both focussed on quartz (Law *et al.*, 1990; Toy *et al.*, 2008).

95 To explore the capabilities of this approach, we conduct a detailed Schmid factor
96 analysis of calcite in marbles deformed within a shear zone of the Karakoram Fault Zone
97 (KFZ), NW India (Figure 1). Calcite is particularly well suited for Schmid factor analysis
98 because: (1) techniques are well established to infer palaeostress magnitudes and orientations
99 (Turner, 1953; Rowe and Rutter, 1990) as well as metamorphic and deformation temperatures
100 (Covey-Crump and Rutter, 1989; Burkhard, 1993) from calcite microstructures; (2) the
101 critical resolved shear stresses (CRSSs) of calcite slip systems are experimentally constrained
102 (De Bresser and Spiers, 1997); and (3) these CRSSs and the post-yield behaviour exhibit low
103 strain rate sensitivity (stress exponents in the ranges 5.3–42.6 and 9.3–15.5, respectively)
104 indicating near plastic (as opposed to strain rate-sensitive viscous) behaviour when deformed
105 at differential stresses greater than approximately 30 MPa (Wang *et al.*, 1996; De Bresser and
106 Spiers, 1997). The marbles that we investigate have undergone a protracted deformation
107 history during exhumation and cooling from upper amphibolite-grade conditions to near
108 surface depths and occur in a fault zone that exhibits geomorphological evidence for M_w 7+
109 earthquakes during the Quaternary (Brown *et al.*, 2002; Rutter *et al.*, 2007; Wallis *et al.*,
110 2013). We investigate the latter part of this history as the rocks were exhumed and cooled
111 through the frictional-viscous transition zone (Wallis *et al.*, 2013, 2015) and underwent a
112 transition from aseismic flow to potentially seismogenic frictional failure (Rutter *et al.*,
113 2007). In particular, we use Schmid factor analysis combined with other microstructural
114 observations to test: (1) the manner in which slip system activity potentially varied under
115 evolving temperature and stress conditions during exhumation, (2) the impact of strain
116 hardening on slip system activity, and (3) how these factors affected the transition from
117 crystal plastic to frictional and potentially seismogenic styles of deformation.

118 2. Geological Setting

119 The KFZ is a > 800 km long fault zone that strikes NW-SE and delineates the western

margin of the Tibetan plateau, accommodating dextral displacement resulting from the India-Asia collision (Figure 1). Along the central KFZ in NW India structures formed at and below lower amphibolite grade are unequivocally attributable to deformation within the KFZ, and record a sequence of fault rocks formed at progressively lower temperature due to ongoing deformation during exhumation (Phillips and Searle, 2007; Wallis *et al.*, 2013, 2015). We investigate marbles deformed within the Pangong strand of the KFZ, adjacent to the Pangong Transpressional Zone (PTZ) (Figure 1).



127

128 **Figure 1**129 *Simplified structural maps of the studied outcrop in the KFZ and wider tectonic context. (a)*

130 and (b) are drawn following Phillips and Searle (2007) and Van Buer *et al.*, (2015). (c) is
131 modified from Rutter *et al.* (2007) and includes their specimen localities and the results of
132 their calcite twinning analysis.

133 Between Muglib and Pangong Tso, the Pangong strand deforms rocks of the Pangong
134 Metamorphic Complex (PMC) and juxtaposes them with the PTZ (Figure 1). The PMC
135 consists of banded marbles, amphibolites, and pelites that underwent regional metamorphism
136 under kyanite grade (up to $736 \pm 47^\circ\text{C}$ and 1059 ± 219 MPa, Wallis *et al.*, 2014) and
137 sillimanite grade conditions (Streule *et al.*, 2009), followed by retrograde metamorphism and
138 KFZ deformation under lower amphibolite to sub-greenschist conditions (Rutter *et al.*, 2007;
139 Streule *et al.*, 2009; Wallis *et al.*, 2014; Van Buer *et al.*, 2015).

140 Rutter *et al.* (2007) studied in detail an outcrop of deformed marble near Muglib
141 ($\text{N}34^\circ00'55''$ $\text{E}078^\circ17'03''$), providing the context for this study (Figure 1). Here we
142 summarise the most relevant findings of their study. Grain-shape foliation at this locality dips
143 moderately SW and mineral stretching lineations plunge gently both NW and SE, consistent
144 with the wider KFZ kinematics. Rutter *et al.* (2007) investigated seven marble samples
145 exhibiting microstructures that record mylonitic fabrics evident as varying degrees of
146 dynamic recrystallisation. From the reconstructed grain size of weakly recrystallised host
147 grains, they estimated metamorphic temperatures in the range $300 \pm 20^\circ\text{C}$ to $480 +130/-30^\circ\text{C}$,
148 using the grain size-temperature relationship of Covey-Crump and Rutter (1989). These data
149 place an upper limit on the temperature of overprinting deformation in each sample. The
150 grain size of dynamically recrystallised neoblasts indicates flow stresses in the range of $40 \pm$
151 20 MPa to 110 ± 40 MPa according to the calibration of Rutter (1995) based on dynamic
152 recrystallisation by grain boundary migration. The choice of this calibration, rather than an
153 alternative based on dynamic recrystallisation by subgrain rotation (Rutter, 1995), is
154 supported by our microstructural analysis in the following sections, which reveals irregular

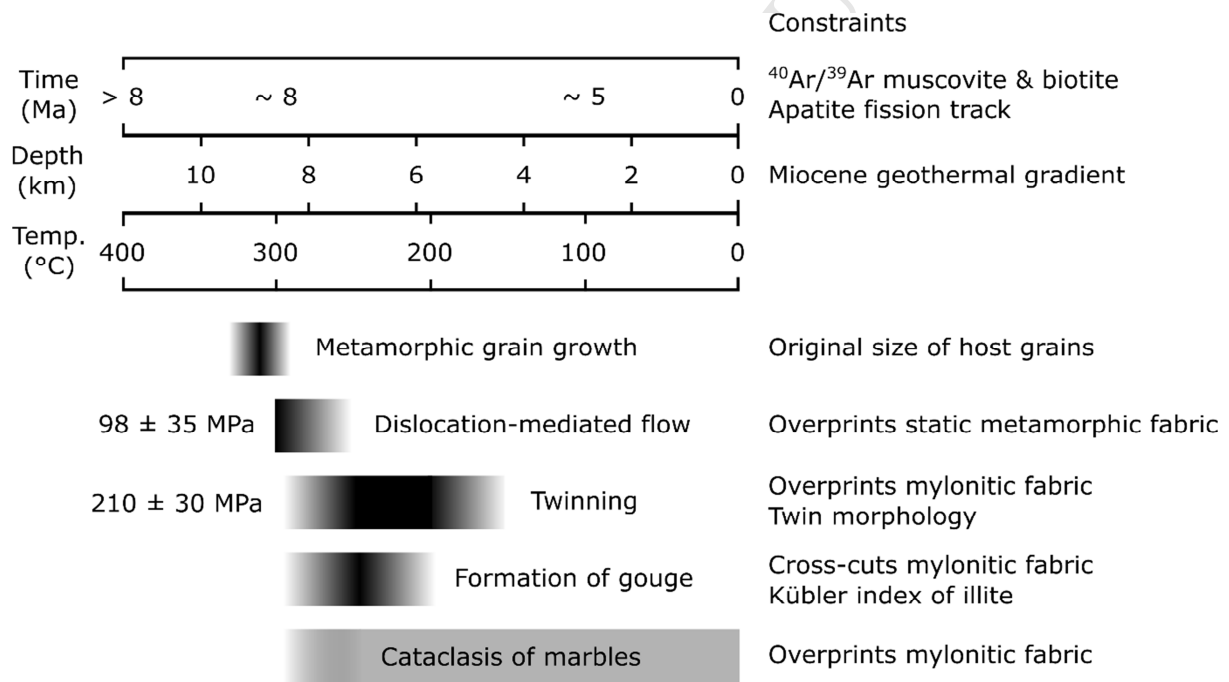
155 grain boundary morphologies but limited subgrain development, consistent with
 156 microstructures reported by Rutter *et al.* (2007). Twin incidence (the percentage of grains, in
 157 a given grain size class interval, that contain optically visible twin lamellae) indicates
 158 differential stresses in the range of 160 ± 30 MPa to 250 ± 30 MPa according to the
 159 calibration of Rowe and Rutter (1990). Thick twins exhibit straight, or curved and tapered
 160 boundaries indicating temperatures of 200–250°C (Burkhard, 1993). These constraints, along
 161 with observations that the mylonitic fabric is cross-cut by calcite veins that are twinned but
 162 not mylonitised, suggest that twinning postdates dynamic recrystallisation (Rutter *et al.*,
 163 2007). Dynamic analysis of calcite twins, using the method of Turner (1953), indicates a
 164 palaeostress state that exerted N-S compression and E-W extension, consistent with
 165 transpressional motion on the NW-SE-trending fault trace, foliation and lineations (Figure 1).

166 **Table 1** *Microstructural data from calcite in EM1 and inferred deformation conditions*
 167 *experienced by sample EM1, from Rutter et al. (2007)*

Parameter	Value	Notes
Host grain size (μm)	240 ± 11	Measured from weakly recrystallised grains where the original grain outline could be established.
Dynamically recrystallised grain size (μm)	40 ± 9	Measured from digital maps of several hundred grains following Rutter (1995).
Overall (host and recrystallised) grain size (μm)	48 ± 10	Measured from digital maps of several hundred grains following Rutter (1995).
Temperature ($^{\circ}\text{C}$)	310 ± 20	From grain size-temperature relationship of marbles on Naxos, Greece, based on Covey-Crump and Rutter (1989). Taken as an approximate upper-bound for the deformation temperature.
Flow stress (differential) (MPa)	98 ± 35	From dynamically recrystallised grain size using the calibration of Rutter (1995).
Twinning stress (differential) (MPa)	210 ± 30	From the twinning incidence piezometric relationship of Rowe and Rutter (1990).

168

169 The marbles at the Muglib locality are locally overprinted by bands of cataclasite and
 170 are cross-cut by a ~10 m thick zone of clay-bearing fault gouge that displays P foliations and
 171 R_1 Riedel shears consistent with dextral KFZ deformation (Figures 1 and 2). The Kübler
 172 index for authigenic illite in the gouge indicates gouge formation at the anchizone-epizone
 173 transition, tentatively taken to be ~300°C (Figure 2; Rutter *et al.*, 2007). The overprinting of
 174 mylonitic textures by cataclastic textures records the transition from crystal plastic
 175 deformation of the marbles to frictional and potentially seismogenic deformation within the
 176 marble cataclasite and clay-rich gouge zone.



177

178 **Figure 2** Summary of constraints on the deformation and exhumation histories of the
 179 investigated marble sample EMI (metamorphic grain growth, dislocation-mediated flow, and
 180 twinning) and the surrounding rocks (formation of gouge and cataclasis). Constraints on
 181 temperatures of deformation and metamorphic processes, along with differential stresses, are
 182 obtained or inferred from Rutter *et al.* (2007). The Miocene geothermal gradient within the
 183 Pangong Transpressional Zone was estimated by Wallis *et al.* (2014) to be ~35°C/km based

184 on geothermobarometry of migmatites formed at ~17 Ma. Time constraints are derived from
185 $^{40}\text{Ar}/^{39}\text{Ar}$ and apatite fission track thermochronology (Boutonnet *et al.*, 2012; Wallis *et al.*,
186 2016b).

187 Thermochronological data from biotite $^{40}\text{Ar}/^{39}\text{Ar}$ (Boutonnet *et al.*, 2012) and apatite fission
188 track (Wallis *et al.*, 2016b) indicate that the Pangong strand and PTZ cooled from ~320°C to
189 ~120°C between ~9 Ma to ~5 Ma (Figure 2). Dynamic recrystallisation of the marbles
190 therefore likely occurred at 7–9 Ma, and deformation twinning at ~6–7 Ma (Figure 2). Offset
191 geological markers indicate long-term average slip rates of 2.7–10.2 mm/yr since ~15 Ma
192 (Phillips *et al.*, 2004).

193 Quaternary deformation on the Pangong strand is recorded by offset debris flows and
194 alluvial fans, which indicate an average slip rate of 4 ± 1 mm/yr since 11–14 ka (Brown *et*
195 *al.*, 2002). These landforms are offset by several metres, indicating the occurrence of
196 earthquakes of $> 7 M_w$, with probable recurrence intervals of ~500–1000 years based on both
197 the ages of the landforms and earthquake scaling relationships (Brown *et al.*, 2002; Wallis *et*
198 *al.*, 2013). Brown *et al.* (2002) inferred that a $7 M_w$ earthquake has occurred on the Pangong
199 strand since 1–2 ka.

200 For this study we focus on mylonitic marble sample EM1 of Rutter *et al.* (2007), for
201 which the deformation conditions are particularly well constrained (Table 1, Figure 2).
202 Notably, this is one of the lowest temperature samples studied by Rutter *et al.* (2007), with
203 the size of host grains placing an upper limit of $310 \pm 20^\circ\text{C}$ on the temperature of formation
204 of the mylonitic fabric (Table 2). This temperature is similar to the temperature of ~300°C
205 estimated for formation of the gouge layer. Therefore, EM1 records mylonitic deformation
206 shortly preceding, or broadly coincident with, the onset of frictional deformation at this
207 structural level. The results derived from detailed analysis of this sample are interpreted in

208 the well-constrained context, outlined above, of evolving deformation processes and
209 conditions as the marbles and surrounding units were exhumed.

210 3. Methods

211 A section of sample EM1 of Rutter *et al.* (2007) was cut parallel to the lineation and
212 perpendicular to the foliation. This section was polished with successively decreasing grit
213 sizes down to 0.25 μm diamond grit, followed by 0.03 μm colloidal silica. Electron
214 backscatter diffraction (EBSD) data were collected on a band of fine-grained matrix calcite
215 using an FEI Quanta 650 FEG E-SEM in the Department of Earth Sciences, University of
216 Oxford. The system is equipped with an Oxford Instruments NordlysNano EBSD camera and
217 AZtec/Channel5 software. Data were collected by automated mapping and consist of 1003 x
218 692 points with a step size of 1 μm . 96.9% of the map area was indexed as calcite, and the
219 majority of points that were not indexed were due to the presence of other phases with rare
220 occurrence, such as quartz. The data were processed to remove individual mis-indexed pixels
221 that had $> 10^\circ$ misorientation from all their neighbours. Next, non-indexed pixels with ≥ 7
222 neighbours belonging to the same grain were filled with the average orientation of their
223 neighbours. Maps of crystal orientation and local misorientation within a 3x3 pixel kernel
224 were produced using Channel5. Pole figures and Schmid factor analyses were computed and
225 plotted using the MATLAB® toolbox MTEX 4.5 (Bachmann *et al.*, 2010; Mainprice *et al.*,
226 2011). Analysis in MTEX utilised the built-in *SchmidFactor* function to operate on
227 *slipSystem* and *stress tensor* MTEX objects (Supplementary Material). These objects were
228 specified as the relevant slip systems for calcite and stress tensor for the natural deformation
229 as described below.

230 The Schmid factor of a slip/twin system describes the fraction of the applied stress
231 that is resolved onto a particular slip/twin plane in the slip/twin direction, and can be

232 described either as a scalar value (Schmid, 1928; Schmid and Boas, 1950) or as a second rank
 233 tensor (e.g. Pokharel *et al.*, 2014). In the conventional definition, originally formulated for
 234 uniaxial tension (Schmid, 1928; Schmid and Boas, 1950), the Schmid factor (m^s) of a
 235 slip/twin system (s) is computed as

$$m^s = \cos\phi\cos\lambda, \quad (1)$$

236 where ϕ and λ are the angles between the maximum principal stress direction and the
 237 slip/twin plane normal and slip/twin direction, respectively. This scalar Schmid factor then
 238 relates the applied differential stress (σ_{diff} , i.e., the difference between the maximum and
 239 minimum principal stresses) to the shear stress resolved on the slip/twin system (τ^s) by

$$\tau^s = m^s\sigma_{\text{diff}}. \quad (2)$$

240 The maximum fraction of the differential stress (σ_{diff}) that can be resolved onto a slip/twin
 241 plane in the slip/twin direction is 0.5. This corresponds to the maximum value of m^s .

242 An alternative approach, which allows analysis of varied stress states, is to employ the
 243 Schmid tensor. The symmetric Schmid tensor (\mathbf{m}^s) describes the projection of the deviatoric
 244 stress tensor ($\boldsymbol{\sigma}$, i.e., with the mean stress subtracted from each normal stress) onto a slip/twin
 245 system (s), defined by unit vectors describing a slip/twin direction (\mathbf{b}^s) and slip/twin plane
 246 normal (\mathbf{n}^s), by

$$\tau^s = \frac{1}{2}(\mathbf{b}^s \otimes \mathbf{n}^s + \mathbf{n}^s \otimes \mathbf{b}^s) : \boldsymbol{\sigma} = \mathbf{m}^s : \boldsymbol{\sigma}, \quad (3)$$

247 which yields the shear stress resolved on that slip system (τ^s) (for a recent review, see
 248 Pokharel *et al.*, 2014). In other words, the components of \mathbf{m}^s determine the fraction of each
 249 component in the deviatoric stress tensor that is resolved onto the slip/twin plane in the
 250 slip/twin direction. In plastically deforming crystals, dislocation glide or twinning can only
 251 occur when τ^s exceeds a threshold value, that is, the critical resolved shear stress (τ_c^s)
 252 (Schmid, 1928; Schmid and Boas, 1950). The value of τ_c varies with slip/twinning system,

253 material, and environmental conditions, primarily temperature (e.g. De Bresser and Spiers,
254 1997; Morales *et al.*, 2014).

255 To calculate Schmid factors for past deformations, constraints on the palaeo-stress
256 state are required. Differential stresses applied to sample EM1 have been estimated from
257 palaeopiezometric analyses (Table 1; Rutter *et al.*, 2007), but the shape of the stress tensor
258 also needs to be determined. Based on the macroscopic kinematics of the Pangong strand,
259 along with asymmetric deformation microstructures and distributions of foliations, lineations,
260 and palaeostress orientations reported by Rutter *et al.* (2007) (Figure 1), we infer that the
261 deformation history of EM1 was dominated by simple shear. To further test the hypothesis
262 that deformation was dominantly simple shear, we apply the approach of Michels *et al.*
263 (2015) to determine the macroscopic vorticity axis from crystallographic orientation data.
264 This method uses principal geodesic analysis of intragranular orientation dispersion to fit a
265 single ‘crystallographic vorticity axis’ (CVA) to each grain. For samples in which dislocation
266 activity accommodated significant strain, CVAs averaged over many grains may record the
267 vorticity axis of deformation.

268 Values of the scalar Schmid factor, m^s , can be computed by entering a normalised
269 stress tensor, $\hat{\sigma}$, in the right hand side of Equation 3 to give

$$m^s = \mathbf{m}^s : \hat{\sigma}. \quad (4)$$

270 Assuming macroscopic simple shear deformation within the Pangong strand, and defining $\hat{\sigma}$
271 as

$$\hat{\sigma} = \sigma / \sigma_{\text{diff}}, \quad (5)$$

272 gives

273

$$\hat{\sigma} = \begin{bmatrix} 0 & 1/2 & 0 \\ 1/2 & 0 & 0 \\ 0 & 0 & 0 \end{bmatrix}. \quad (6)$$

274 This formulation denotes that the maximum possible value of the shear stress components is
 275 half the magnitude of the applied differential stress. This approach is equivalent to that of
 276 Law *et al.* (1990), except that they normalised the shear stress components by their maximum
 277 possible magnitude, which leads to non-zero terms in $\hat{\sigma}$ having a value of one and m with
 278 values in the range 0–1. In contrast, by normalising the shear stress components by the
 279 magnitude of the differential stress, we obtain values of m in the conventional range 0–0.5,
 280 which can be used more directly in conjunction with differential stress magnitudes from
 281 palaeopiezometry. If crystal orientations can be mapped across the microstructure and the
 282 differential stress measured or inferred, then the scalars τ^s and m^s can be mapped across the
 283 microstructure.

284 To determine which of the calcite slip systems could potentially be activated by the
 285 palaeostresses, we transform the normalised stress tensor, $\hat{\sigma}$, in Equation 6, into the crystal
 286 coordinate system of each measured orientation and compute m^s for each slip system. This
 287 stress tensor, $\hat{\sigma}$, and Schmid tensor, m^s , allow calculation of m^s by Equation 4. Values of m^s
 288 are multiplied by σ_{diff} to calculate the corresponding shear stress, τ^s , resolved on each slip
 289 system according to Equation 2. In crystals with multiple symmetrically equivalent variants
 290 of each slip/twin system, such as calcite, the variant with the highest value of m^s will
 291 slip/twin at the lowest applied stresses.

292 Once the Schmid factor and resolved shear stress for each slip system have been
 293 calculated, it is necessary to assess whether the applied stress was sufficient to activate
 294 dislocation glide, i.e., whether $\tau^s > \tau_c^s$. The experimental work on calcite single crystals and
 295 data compilation of De Bresser and Spiers (1993, 1997) established the operative calcite slip
 296 and twinning systems and their absolute CRSSs over the temperature range 20–800°C.

297 Therefore, we take the values of τ_c for $\{e\}$ -twinning and dislocation slip on the $\{r\}$ - and $\{f\}$ -
 298 planes, for temperatures of 200°C and 300°C, from De Bresser and Spiers (1997) (Table 2).
 299 These temperatures approximately correspond to the lower- and upper-bounds for
 300 temperature constrained by the geological context (Section 2), for the occurrence of twinning
 301 and dynamic recrystallisation respectively in sample EM1. We use values of τ_c for the variant
 302 of the $\{f\}$ slip system active at $\leq 300^\circ\text{C}$ (i.e., $\{-1012\}\langle 2-201\rangle$), rather than the variant active
 303 at $\geq 500^\circ\text{C}$ (i.e., $\{-1012\}\langle -101-1\rangle$) in the experiments of De Bresser and Spiers (1997).
 304 These experiments demonstrated that values of τ_c for calcite slip systems depend little on
 305 strain rate (stress exponents in the range 5.3–42.6), which reduces the uncertainty associated
 306 with applying them to analyse deformation that occurred at lower strain rates than the
 307 deformation experiments. The range of values of τ_c for slip on the $\{r\}$ system at 300°C,
 308 reported by De Bresser and Spiers (1997), is on the order of 20 MPa. As this range is smaller
 309 than the uncertainties of the palaeopiezometric stress estimates for the nature samples (30–35
 310 MPa, Table 1, Rutter *et al.*, 2007), we consider only the best-fit values of τ_c at each
 311 temperature, interpolated from the fits reported by De Bresser and Spiers (1997), to make
 312 simple first-order comparisons. From the critical resolved shear stresses constrained by
 313 experiments (De Bresser and Spiers, 1997) and from the applied differential stresses
 314 constrained by palaeopiezometry (Rutter *et al.*, 2007), we compute the minimum value of m^s
 315 (i.e. m_{\min}) necessary to initiate twinning or dislocation glide on each system by

$$m_{\min} = \tau_c / \sigma_{\text{diff}}, \quad (7)$$

316 (Table 2).

317 **Table 2** Summary of slip system information for EM1

Deformation temperature (°C)	Slip system	τ_c (MPa)	Applied differential stress (MPa)	Minimum m for twinning/dislocation glide
------------------------------	-------------	----------------	-----------------------------------	--

300	{ <i>e</i> }-twinning {-1018}<40-41>	2	98 ± 35	0.02
300	{ <i>r</i> }-slip {10-14}<-2021>	22	98 ± 35	0.22
300	{ <i>f</i> }-slip {-1012}<2-201>	52	98 ± 35	0.53
200	{ <i>e</i> }-twinning {-1018}<40-41>	3	210 ± 30	0.01
200	{ <i>r</i> }-slip {10-14}<-2021>	41	210 ± 30	0.20
200	{ <i>f</i> }-slip {-1012}<2-201>	77	210 ± 30	0.37

318

319 By computing maps of m^s , we are able to determine which grains have $m > m_{\min}$ (and
320 $\tau^s > \tau_c^s$) and therefore estimate the area fraction of grains that can deform by each deformation
321 mode under the applied palaeostress conditions. We also perform this analysis for applied
322 stresses throughout the range 1–250 MPa to explore the effects of increasing stress acting on
323 the mapped microstructure at 300°C and 200°C. An MTEX script to carry out these
324 procedures is included as Supplementary Material.

325 An important caveat to the analysis described here is that the stress state would need
326 to be homogeneous throughout the material for the point-by-point Schmid factors to be
327 reliably accurate. However, micromechanical models of viscoplastic deformation that
328 explicitly account for detailed microstructures suggest that stress and strain vary significantly
329 among grains and are even distributed heterogeneously within grains (e.g. Pokharel *et al.*,
330 2014). Heterogeneous distributions of stress and strain arise due to the elastic and plastic
331 anisotropy of individual grains and local grain-grain interactions. Such heterogeneities have
332 been recently observed in experimentally deformed Carrara marble (Quintanilla-Terminel

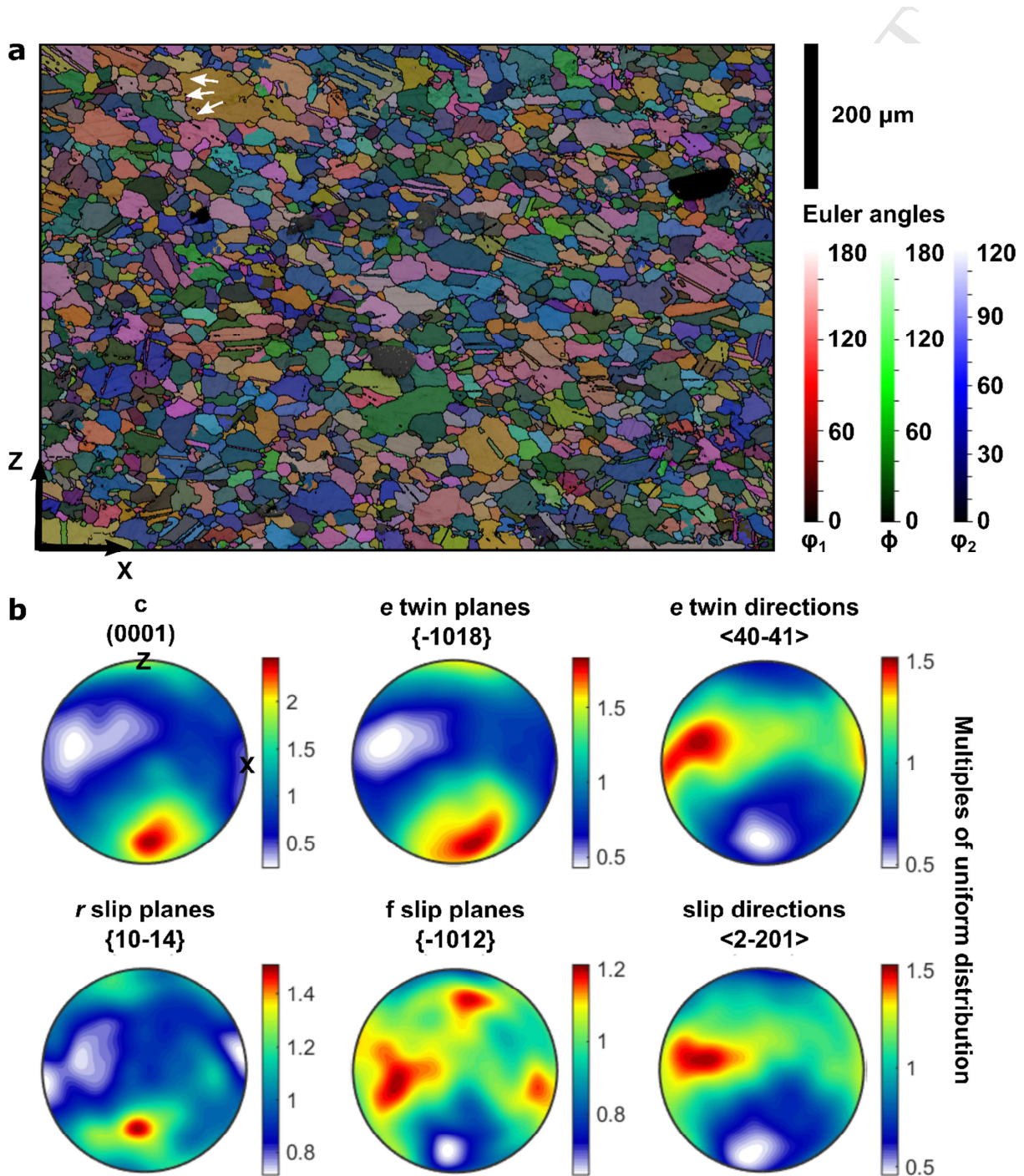
333 and Evans, 2016). Thus, rather than interpreting the behaviour of specific individual points or
334 grains, we take the approach of considering the distribution of Schmid factors and predicted
335 slip/twin system activity over ~2500 grains, providing an averaged estimate of the slip system
336 activity across the bulk material. We suggest that these averaged values of slip system
337 activity are more reliable than the results for individual grains displayed in the maps because
338 the stress states averaged throughout the rock volume must equal the macroscopic applied
339 stress state. The Schmid factor approach offers a simple method to consider a larger number
340 of grains than would be possible using more advanced computational techniques that include
341 stress heterogeneity.

342 During progressive deformation, Schmid factors define only an instantaneous
343 relationship between stress and crystal orientation, as ongoing crystal rotations continuously
344 modify the Schmid factors for each slip system in aggregates deforming by dislocation glide.
345 Therefore, Schmid factors calculated from the microstructure of an exhumed rock indicate
346 which slip systems would have been well aligned for dislocation glide during the *next*
347 increment of slip (which *ipso facto* never occurred). In contrast, use of mapped Schmid
348 factors to interpret prior deformation that led to formation of the observed microstructure is
349 more complex and requires additional assumptions/constraints regarding microstructural
350 evolution (particularly grain rotations) or steady state. Therefore, Schmid factor analysis is
351 well suited to our application, in which the mylonitic microstructure records a snapshot
352 formed at ~300°C as the dislocation-mediated processes that formed it ceased to operate, and
353 in which our aim is to investigate the controls on the *subsequent* evolution of deformation
354 processes.

355 **4. Results**

356 The measured CPO is consistent with the inference of simple shear deformation.

357 Calcite $\{c\}$, $\{e\}$ and $\{r\}$ poles are clustered in point maxima near the foliation normal,
 358 whereas the twin and slip directions are weakly girdled with superimposed point maxima
 359 close to the lineation direction (Figure 3). The CPO of $\{f\}$ planes is weak, with three low
 360 intensity maxima (Figure 3b).

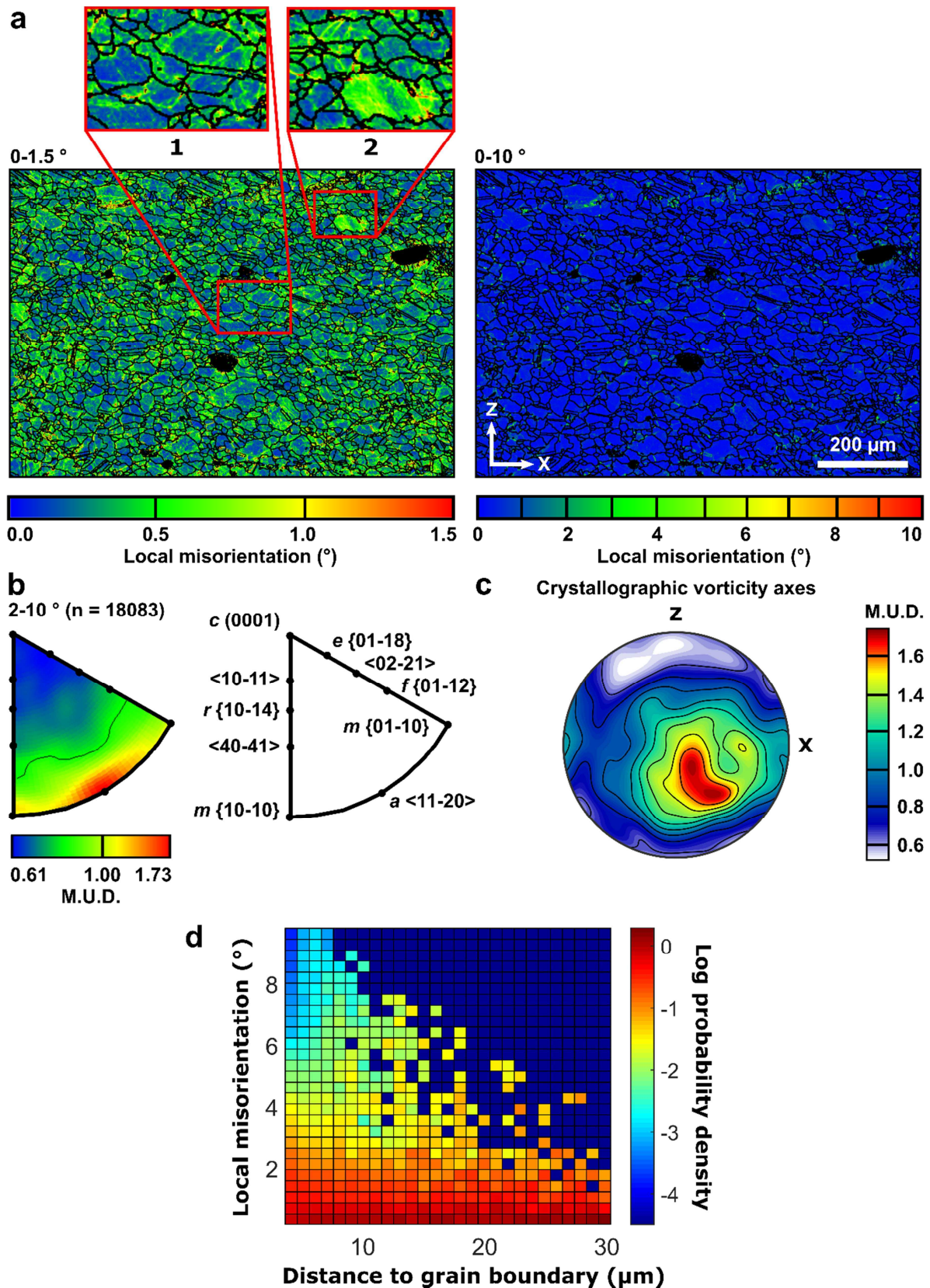


361

362 **Figure 3** Crystal orientation data from EBSD analysis of sample EM1. (a) Map of crystal

363 orientations colour-coded using Euler angles in the convention of Bunge (1982),
364 superimposed on a grey-scale map of diffraction pattern band contrast. Black lines mark
365 boundaries of $\geq 10^\circ$ misorientation between adjacent pixels. White arrows indicate an
366 example of a lobate and irregular grain boundary. (b) Lower hemisphere pole figures of
367 crystal planes and directions relevant to the calcite slip and twin systems considered. X
368 indicates the lineation and Z the foliation normal. Shear sense is top-to-right.

369 Crystallographic misorientation data indicate that relatively few subgrain boundaries
370 with misorientations in the range $1\text{--}10^\circ$ are present (Figure 4a), but the inverse pole figure of
371 misorientation axes demonstrates that those subgrain boundaries that are present have
372 rotation axes parallel to the $a\langle 11\text{-}20 \rangle$ directions (Figure 4b). The map of local
373 misorientations scaled from $0\text{--}1.5^\circ$ reveals the presence of abundant low-angle
374 misorientations of $\sim 1^\circ$ (Figure 4a). These misorientations are arranged in networks of low-
375 angle subgrain boundaries and regions of more distributed lattice curvature. The portions of
376 grains close to grain boundaries have greater local misorientation relative to the interior,
377 representing higher dislocation densities, than grain interiors (Figure 4a,d). The visible
378 microstructure indicates that the measurements are generally above the background noise
379 level, despite the small misorientation angles. Crystallographic vorticity axes are generally
380 aligned sub-perpendicular to both the lineation and foliation normal, consistent with
381 dominantly simple shear (Figure 4c; Michels *et al.*, 2015). This observation provides
382 independent support for our choice of stress state (i.e. Equation 6) used for Schmid factor
383 analysis.



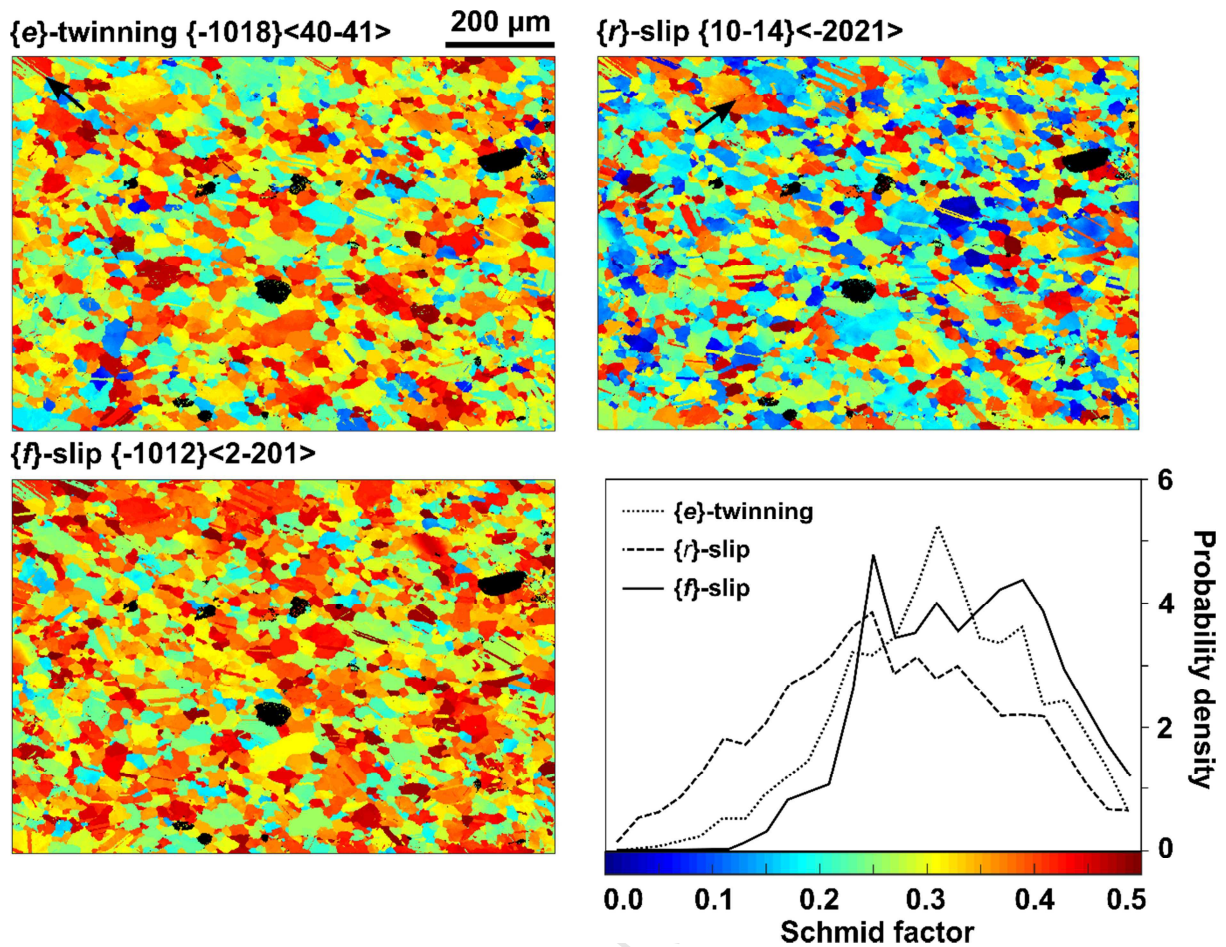
384

385 **Figure 4** Misorientation analysis of EMI. (a) Maps of local misorientation within 3x3 pixel

386 kernels, scaled for two ranges of misorientation angle. Grain and twin boundaries are

387 overlaid as black lines. Region 1 exhibits higher values of misorientation concentrated near
388 grain boundaries. Region 2 shows both subgrain boundaries (top left) and more widespread
389 misorientation (lower right). (b) Inverse pole figure presents the orientation of misorientation
390 axes of subgrain boundaries in the crystal reference frame. (c) Stereoplot illustrating
391 contoured crystallographic vorticity axes (one axis per grain), determined using the method
392 of principal geodesic analysis of intragranular dispersion (Michels et al., 2015). X indicates
393 the lineation and Z the foliation normal. (d) Probability density functions (PDFs) of local
394 misorientation in $1\ \mu\text{m}$ bins of Euclidean distance to grain boundary (including twin
395 boundaries) within the 2-D EBSD map plane, i.e. each column is a different PDF. This
396 plotting approach addresses the bias of having different numbers of points at each distance
397 by allowing PDFs to be compared between different distances. Local misorientation was
398 calculated within a 3×3 pixel kernel. Only points at distances $> 3\ \mu\text{m}$ from a grain boundary
399 are plotted to avoid processing artefacts in kernels that include boundaries. Grain
400 boundaries were defined as $>10^\circ$ misorientation.

401 Maps of Schmid factor show grain-by-grain variations in the maximum Schmid factor
402 of each family of slip systems (Figure 5). Each family of slip systems exhibits a wide range
403 of Schmid factors within the map area (Figure 5). The probability densities of Schmid factors
404 exhibit similar general form between each slip system, being skewed towards high Schmid
405 factors. The distribution describing Schmid factors for slip on $\{f\}$ -planes is most heavily
406 skewed towards high values (Figure 5). Schmid factors vary between twins and host grains,
407 evident as stripes of different Schmid factor. More subtle variations in Schmid factor are
408 apparent across subgrain boundaries.

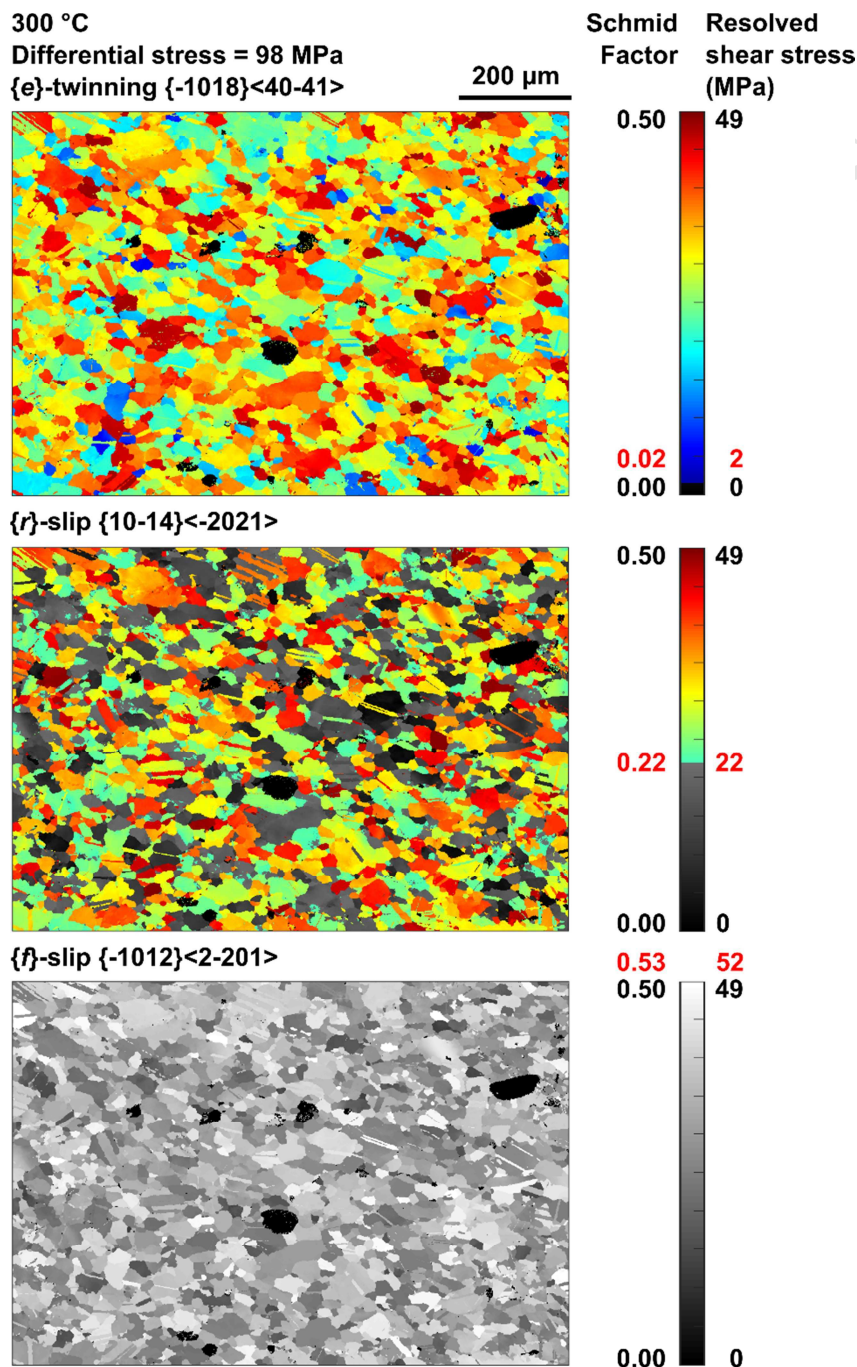


409

410 **Figure 5** Maps and probability density plots of Schmid factor for each calcite slip/twin
 411 system. Probability densities were calculated for bins of 0.02 width. The black arrow in the
 412 upper-left of the map of Schmid factor for $\{e\}$ -twinning indicates an example of changes in
 413 Schmid factor across twin boundaries. The black arrow in the upper-left of the map of
 414 Schmid factor for $\{r\}$ -slip indicates an example of changes in Schmid factor across a
 415 subgrain boundary.

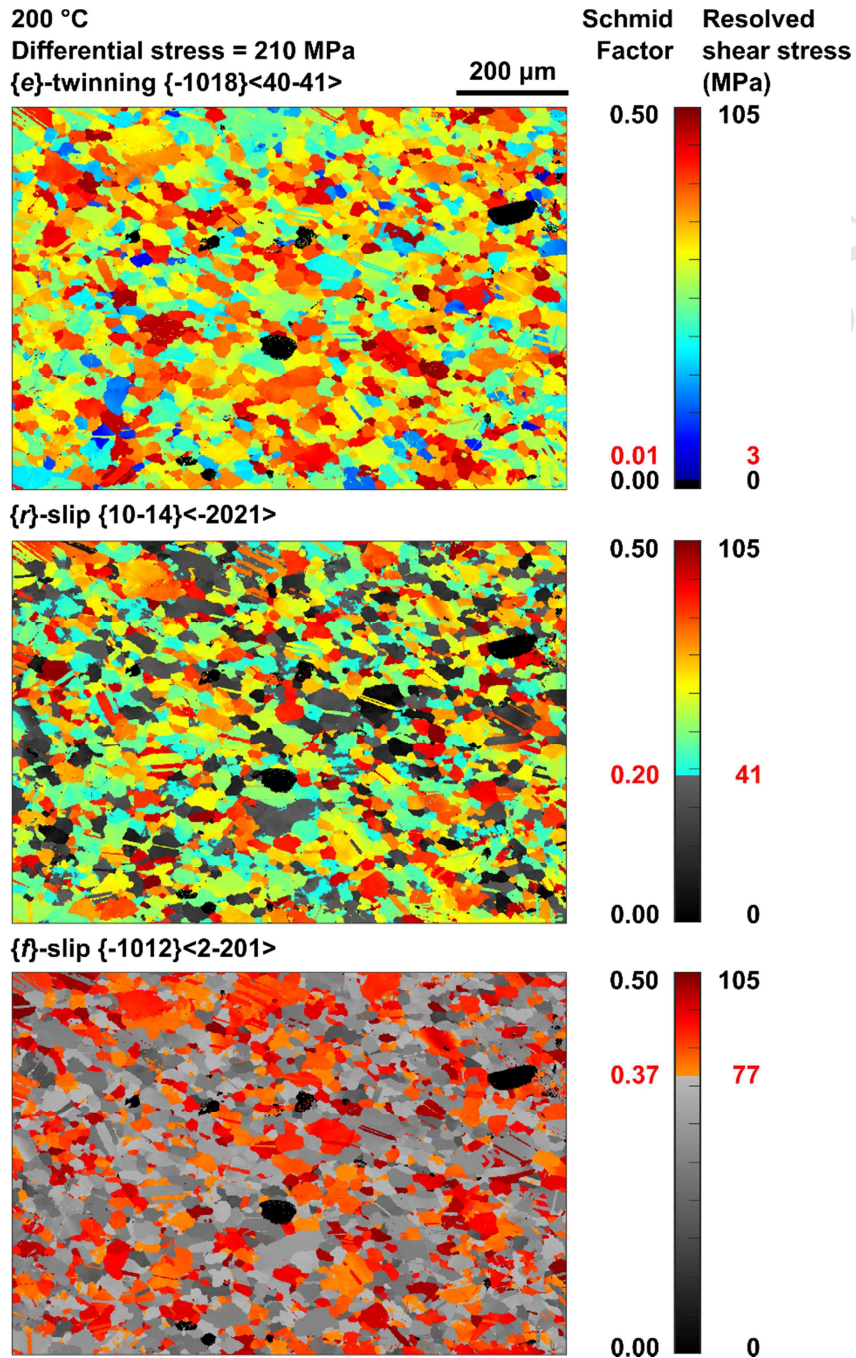
416 The apparent proportions of grains that can deform by each slip/twin system vary
 417 across the temperature and stress ranges within which deformation is inferred to have taken
 418 place (figures 6–8). At 300°C and a piezometric stress of 98 MPa, none of the grains can
 419 deform by $\{f\}$ -slip because τ_c (52 MPa) is greater than 0.5 of the applied stress (figures 6 and
 420 8a, Table 2). However, within the upper-bound uncertainty of the stress estimate, up to 29%

421 of the microstructure can deform by $\{f\}$ -slip (Figure 8a). Within the stress uncertainty, 63
 422 +18/-39% can deform by $\{r\}$ -slip and 100% can deform by $\{e\}$ -twinning (figures 6 and 8a).
 423 At 200°C and the higher stress conditions estimated from twinning incidence, 39 +17/-25%
 424 should be able to deform by $\{f\}$ -slip and 72 +7/-10% should be able to deform by $\{r\}$ -slip
 425 (figures 7 and 8b). Again 100% of the grain area exceeds the critical resolved shear stress for
 426 $\{e\}$ -twinning (Figures 7 and 8b).



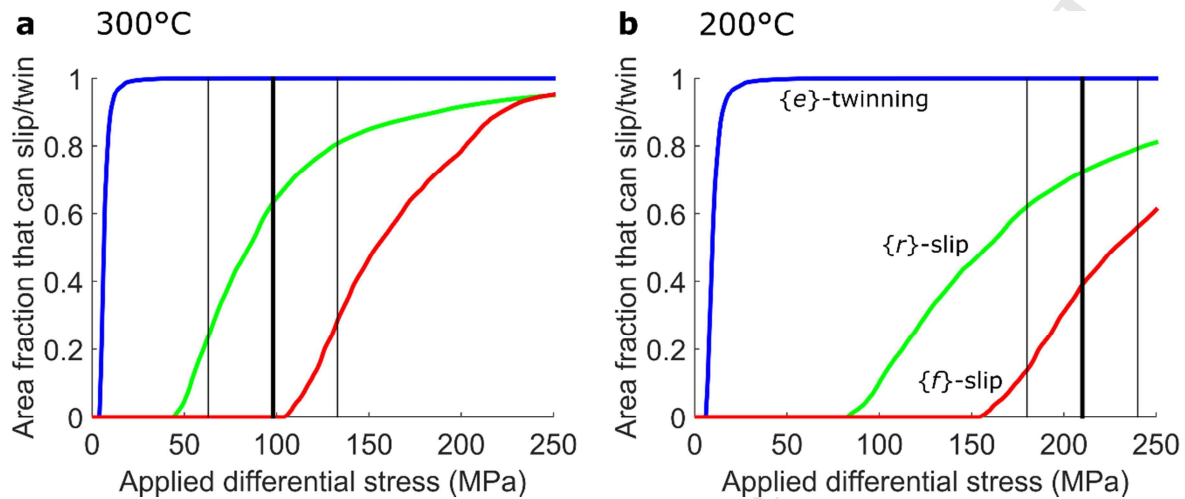
427

428 **Figure 6** Maps of grains that exceed the minimum Schmid factor necessary to initiate
 429 twinning or dislocation glide at 300°C and the stress determined from dynamically
 430 recrystallised grain size. The minimum Schmid factor and corresponding critical resolved
 431 shear stress are marked in red beside the colour bar. Areas above and below this threshold
 432 are represented by colour-scale and grey-scale respectively.



434 **Figure 7** Maps of grains that exceed the minimum Schmid factor necessary to initiate

435 twinning or dislocation glide at 200°C and the stress determined from twinning incidence.
 436 The minimum Schmid factor and corresponding critical resolved shear stress are marked in
 437 red beside the colour bar. Areas above and below this threshold are represented by colour-
 438 scale and grey-scale respectively.



439
 440 **Figure 8** Area fraction of grains in mapped microstructure that can deform by
 441 twinning/dislocation glide at (a) 300°C and (b) 200°C, under applied differential stresses
 442 ranging from 0–250 MPa. The stress estimates are determined from (a) dynamically
 443 recrystallised grain size (at ~300°C) and (b) twinning incidence (at 200–250°C) and are
 444 marked by vertical bold black lines with uncertainties marked by fine black lines.

445 5. Discussion

446 5.1. Effects of changing temperature and stress on slip system activity

447 This study constitutes a detailed examination of the microstructure of a single sample
 448 of marble, EM1, deformed by dislocation glide and twinning whilst the Pangong
 449 Metamorphic Complex, within which it was situated, was exhumed through the frictional-
 450 viscous transition zone at temperatures of approximately 200–300°C around 7–8 Ma (Rutter
 451 *et al.*, 2007; Wallis *et al.*, 2013, 2016b). Although this sample represents only a small volume

452 of the fault zone material, the surrounding rocks, which include a wide range of fault rock
453 types formed under varied conditions, provide a well-documented context (Rutter *et al.*,
454 2007) in which to interpret the changing styles of deformation in both sample EM1 and the
455 unit as a whole (Figures 1 and 2). In particular, the frictional fault rocks, i.e. marble
456 cataclasites and clay-rich gouge, are more spatially localised than the mylonitic marbles that
457 they overprint (Figure 1; Rutter *et al.*, 2007). Therefore, microstructural evidence for earlier
458 deformation mechanisms and processes, such as the recrystallised microstructure indicative
459 of dislocation-mediated deformation in EM1, remains preserved and available for analysis,
460 whilst the subsequent switch to frictional failure of the adjacent rocks can be inferred from
461 the locally overprinting frictional fault rock types. The Kübler index of illite in the clay-rich
462 gouge layer suggests that it formed at up to approximately 300°C and therefore closely post-
463 dated mylonitisation, which ceased at approximately 300°C (Figure 2; Rutter *et al.*, 2007). As
464 such, formation of the gouge was broadly coincident with twinning in the mylonitic marbles,
465 which occurred at approximately 200–250°C (Figure 2, Burkhard, 1993). Similarly, the
466 mylonitic marbles are fragmented and overprinted by cataclasites in a zone tens of metres
467 wide adjacent to the gouge layer (Figure 1; Rutter *et al.*, 2007). The fragmented marbles
468 contain relict microstructures indicative of partial dynamic recrystallisation by grain
469 boundary migration prior to cataclasis (Rutter *et al.*, 2007). Therefore, cataclasis must also
470 have occurred after mylonitisation and been broadly coincident with, or more recent than,
471 formation of the gouge layer and twinning in the mylonites (Figure 2). As the mylonitic
472 fabric of EM1 formed at temperatures similar to or only slightly above those at which
473 frictional deformation commenced in the adjacent rocks, we infer that the mylonitic
474 microstructure of the sample remained largely unmodified during subsequent exhumation.
475 We also note that EM1 is located close to the boundary between the mylonitic and
476 fragmented marbles and therefore is well suited (in both spatial location and timing of

477 formation of its deformation fabric) to recording the transition between dislocation-mediated
478 and frictional deformation. These relationships allow us to examine one sample in detail
479 whilst also considering the significance of the deformation processes in the evolution of the
480 rock unit more widely.

481 The predicted changes in slip system activity in EM1 (Figure 8) reflect the combined
482 influence of changing stress and temperature conditions as the rock was exhumed. The
483 decrease in temperature from 300°C to 200°C increases values of τ_c by factors of 1.5–1.9
484 (Table 2), acting to inhibit dislocation glide. However, palaeopiezometric estimates suggest
485 that, at the same time, the applied stress increased by a factor of ~2.1 (Rutter *et al.*, 2007). As
486 a result, a greater fraction of the microstructure appears to have potential to deform by
487 dislocation glide at 200°C and 210 ± 30 MPa than at 300°C and 98 ± 35 MPa (Figures 6–8).
488 This effect is particularly pronounced for $\{f\}$ -slip, which has the highest τ_c . The 98 ± 35 MPa
489 applied stress at 300°C is generally insufficient for slip on $\{f\}$ -planes, whereas, at 200°C and
490 210 ± 30 MPa, 39 +17/-25% of the microstructure exceeds τ_c for $\{f\}$ -slip (Figure 8).
491 However, these findings are superficially at odds with other microstructural and structural
492 features that indicate dislocation activity was greater at higher temperature. Within the
493 sample, dynamically recrystallised grains formed under the lower stress, higher temperature
494 conditions, and were not overprinted by further dynamic recrystallisation under the
495 subsequent higher stress, lower temperature conditions (Figure 2; Rutter *et al.*, 2007). More
496 widely in the rock unit, the mylonitic textures formed at the higher temperatures are
497 overprinted by cataclasites and gouges formed at similar and lower temperatures (Figure 2;
498 Rutter *et al.*, 2007). One possible explanation for the discrepancy between the predictions of
499 slip system activity (Figure 8) and the observed (micro)structural evolution is that the stresses
500 predicted from twinning incidence by the palaeopiezometer of Rowe and Rutter (1990) are
501 inaccurate. This method for estimating past stresses is fully empirical and lacks a detailed

502 microphysical basis often used to support application of laboratory-derived relationships to
503 natural contexts. However, the predicted stresses would have to be in error by approximately
504 a factor of two, or approximately 100 MPa, to preclude slip on the $\{r\}$ system in well
505 oriented grains (Figure 8). Therefore, in the following section, we discuss in more detail the
506 evolution of deformation processes as the rock cooled during exhumation to explore the
507 possibility that microphysical processes are responsible for lack of significant dislocation
508 glide under the low temperature and high stress conditions.

509 **5.2. Evolution of deformation mechanisms during exhumation through the frictional- 510 viscous transition zone**

511 Calcite microstructures in EM1 (this study) and the other samples reported by Rutter
512 *et al.* (2007) include lobate grain boundaries (Figures 3 and 4), porphyroclasts with fine
513 grained mantles (Rutter *et al.*, 2007), and subgrain boundaries (Figure 4). These
514 microstructural observations indicate deformation by dislocation motion, accompanied by
515 dynamic recrystallisation due to grain boundary migration and (to a lesser extent) subgrain
516 rotation (Figures 3 and 4; Rutter *et al.*, 2007). Crosscutting relationships and contrasting
517 palaeopiezometric estimates indicate that these microstructures formed close to the upper
518 bound temperature of $310 \pm 20^\circ\text{C}$ for EM1, constrained by the (now partially overprinted)
519 equilibrium grainsize (Figure 2; Rutter *et al.*, 2007).

520 The general scarcity of subgrain boundaries with misorientations of several degrees or
521 more (Figure 4) indicates that dislocation climb was limited at these temperatures and/or that
522 recovery of intracrystalline strain occurred by other processes, such as cross-slip, dislocation
523 annihilation or climb into high-angle grain boundaries and grain-boundary migration (de
524 Bresser and Spiers, 1990; Liu and Evans, 1997). Misorientation analysis of the few subgrain
525 boundaries that are present indicates that they mostly involve lattice rotations around axes

526 parallel to $a\langle 11-20 \rangle$. Bestmann and Prior (2003) demonstrated that misorientation axes
527 parallel to $\langle a \rangle$ in calcite cannot represent twist boundaries due to the lack of appropriate
528 screw dislocation types in calcite. They also suggested that a precisely defined misorientation
529 axis could result from coupled activity of glide in two co-planar directions, but that this is
530 unlikely in general as it requires an equal contribution from both slip directions. Rather, the
531 misorientation axes are consistent with tilt boundaries constructed of edge dislocations on the
532 $r\{10-14\}\langle -2021 \rangle$ or $f\{-1012\}\langle 10-11 \rangle$ slip systems (Bestmann and Prior, 2003). However, as
533 $f\{-1012\}\langle 10-11 \rangle$ is the high temperature form of $\{f\}$ -slip, active above 500°C in the
534 experiments of De Bresser and Spiers (1997), dislocations on this slip system are unlikely to
535 have formed the subgrain boundaries in EM1. Edge dislocations on the low temperature $\{f\}$ -
536 slip system, $f\{-1012\}\langle 2-201 \rangle$, which we have analysed here, do not generate lattice rotations
537 around $\langle a \rangle$ and therefore also cannot form the subgrain boundaries in EM1. We infer
538 therefore that the subgrain boundaries are constructed of edge dislocations on the $r\{10-14\}\langle -$
539 $2021 \rangle$ slip system. This interpretation is consistent with the estimate that ~63–72% of the
540 microstructure had sufficient resolved shear stress for slip on $r\{10-14\}\langle -2021 \rangle$ across the
541 range of conditions investigated (Figure 8). These conclusions are similar to those reached by
542 Bestmann and Prior (2003), who investigated calcite deformed at temperatures in the range
543 ~300–350°C.

544 The marble mylonites are sequentially overprinted by more localised marble
545 cataclasite and the clay-bearing gouge zone (Figures 1 and 2; Rutter *et al.*, 2007). These
546 cross-cutting relationships and associated microstructures indicate that, as temperature
547 decreased during exhumation, stress increased sufficiently that the frictional failure strength
548 of the rock was exceeded. This onset of frictional deformation occurred after mylonitisation
549 at ~300°C and before, or broadly coincident with, development of the preserved set of twins
550 in the marble (200–250°C, Figure 2; Rutter *et al.*, 2007). We provide additional insight

551 through our Schmid factor analysis, which demonstrates that the calcite would still have had
552 sufficient resolved shear stress for dislocation glide in most crystal orientations *if* CRSS
553 values taken from the yield points in single crystal experiments are applicable to the natural
554 microstructure. The resolved shear stress appears sufficient for considerable dislocation glide
555 even at the lower temperatures of 200–250°C (Figures 7 and 8) at which only twinning and
556 frictional failure occurred (Rutter *et al.*, 2007). In fact, the predictions of slip system activity
557 (Figure 8) indicate that the applied shear stress would have to have been approximately half
558 of the value measured by twinning incidence to de-activate $\{r\}$ -slip in a significant portion of
559 the microstructure.

560 It is important to note that the τ_c values upon which this analysis is based were
561 experimentally determined for relatively low strains of just a few percent ($\leq 4.3\%$, De Bresser
562 and Spiers, 1997). De Bresser and Spiers (1997) recognized significant strain hardening in
563 their experiments, such that the CRSS obtained from yield point stresses effectively places a
564 minimum bound on the resolved shear stress required for further dislocation glide on the
565 corresponding slip system at higher strains. This observation led De Bresser and Spiers
566 (1997) to suggest that strain hardening on the first slip system to activate (i.e., $\{r\}$ -slip) could
567 lead to a strain-induced transition to a different dominant slip system (e.g., $\{f\}$ -slip).

568 Strain hardening in calcite during cooling is likely the result of a reduction in the
569 efficiency of thermally activated intracrystalline strain recovery processes such as cross slip
570 or dislocation climb into either static or migrating twin, subgrain, and grain boundaries
571 (Rutter, 1974; De Bresser and Spiers, 1990; Kennedy and White, 2001). As a result,
572 dislocation interactions and long-range stress fields associated with accumulations of blocked
573 dislocations would have inhibited further dislocation glide (Fleck *et al.*, 1994; Renner *et al.*,
574 2002). Two lines of microstructural evidence support this interpretation. The widespread

575 occurrence of subgrain boundaries with low misorientation angles of approximately $0.5\text{--}1.0^\circ$
576 (Figure 4) suggests that significant dislocation content is present but that dislocations could
577 not organise into lower-energy structures. Similarly, misorientation angles, and hence
578 dislocation content, generally increase towards grain boundaries (Figure 4) suggesting that
579 dislocation climb into boundaries and grain-boundary migration were relatively inefficient
580 compared to the rate of dislocation accumulation.

581 Renner *et al.* (2002) suggested that calcite commonly exhibits a Hall-Petch
582 relationship whereby strength increases with decreasing grain size because back-stresses from
583 dislocations accumulated near grain boundaries inhibit further dislocation glide. This model
584 is consistent with the microstructural observations (orientation gradients generally increasing
585 towards grain boundaries) and mechanical inferences (occurrence of strain hardening) of this
586 study. Kennedy and White (2001) reached similar conclusions based on observations of
587 calcite naturally deformed at relatively low temperatures of $150\text{--}250^\circ\text{C}$. Microstructures in
588 their samples indicated that coarse-grained vein calcite that crystallised with low dislocation
589 densities was able to deform by dislocation glide, whereas finer-grained mylonitic matrix
590 exhibited high densities of tangled dislocations and was interpreted to have strain-hardened.
591 We suggest therefore that the transition from dislocation-mediated flow to frictional failure
592 was promoted by work hardening due to low efficiency of recovery processes, particularly
593 slow climb into grain boundaries, rather than simply the temperature-dependency of critical
594 resolved shear stresses, as the rocks cooled during exhumation. This inference is consistent
595 with experimental observations that strain hardening is more pronounced at lower
596 temperatures for both single crystals (de Bresser and Spiers, 1993, 1997) and aggregates
597 (Rutter, 1974). The predictions of slip system activity (Figure 8) suggest that strain hardening
598 must have imposed additional resistance to glide of at least tens of MPa to prevent large
599 fractions of the microstructure deforming by $\{r\}$ -slip.

600 Microstructures indicative of frictional deformation are preserved within both the
601 cataclastic marbles and the phyllosilicate-rich gouge band (Figure 1; Rutter *et al.*, 2007). As
602 Quaternary earthquakes of magnitude 7+ are recorded by offset alluvial fans and debris flows
603 within 2 km of the sample site (Brown *et al.*, 2002; Rutter *et al.*, 2007), it is pertinent to
604 consider the extent to which the exhumed cataclastic fault rocks record seismogenic
605 processes as an analogue for those occurring at depth. Phyllosilicate-rich gouges typically
606 exhibit velocity-strengthening behaviour and therefore are unfavourable in general for
607 nucleation of earthquake ruptures (Ikari *et al.*, 2011). However, carbonate rocks exhibit
608 strong velocity weakening (Han *et al.*, 2010), and therefore the fragmented marble band was
609 likely capable of nucleating unstable earthquake ruptures whilst at depth. In this case, one
610 important consequence of strain hardening may be to result in the onset of seismogenic
611 deformation at the structural levels at which rocks are exhumed and cooled from $\sim 300^{\circ}\text{C}$ to
612 $\sim 200\text{--}250^{\circ}\text{C}$. We suggest that the processes recorded in the presently exposed fault rocks of
613 the Pangong strand are likely analogous to those occurring at depth, where similar rocks of
614 the PMC continue to be exhumed through the frictional-viscous transition zone.

615 In the case of the KFZ, cooling through the frictional-viscous transition zone was due
616 to ongoing deformation during erosional exhumation (Wallis *et al.*, 2016b). However, the
617 processes documented in this study may also be important in controlling transitions in
618 deformation mechanism and the onset of seismogenic behaviour in other tectonic settings. In
619 particular, carbonate units are commonly dissected by extensive normal fault systems in
620 which tectonic exhumation of footwalls may contribute to cooling (Smith *et al.*, 2011; Cowie
621 *et al.*, 2017). The processes of strain hardening leading to frictional failure may be important
622 controls on the depth of seismicity and strength of the extending mid-crust in such settings.
623 An implication of this finding is that the depth extent of the dominantly frictional upper crust,
624 where earthquakes typically nucleate, potentially varies in both space and time in response to

625 the evolving strain state of rocks in the mid-crust.

626 **5.3. Schmid factor analysis as a tool for analysing crystal plasticity**

627 Schmid-factor analysis provides several useful insights in addition to those that can be
628 gained from more commonly used methods of slip system analysis. Schmid factor maps
629 provide an extension of common CPO analysis by allowing populations of crystal
630 orientations to be readily related directly to specific microstructural elements (e.g. Figures 5–
631 7). This approach is similar to plotting EBSD maps colour-coded using inverse pole figures,
632 except that Schmid factor maps consider the complete crystallography (i.e. angular
633 relationships involving both the slip direction and slip plane normal) rather than individual
634 crystal directions, and relate this explicitly to a stress state of interest (which is often only
635 implied in other approaches).

636 Schmid factor mapping is also the first step to more detailed quantitative analysis of
637 slip system activity, which requires a range of geological (e.g. stress and temperature) and
638 experimental (e.g. CRSS and strain rate sensitivity) constraints. In these respects, calcite is
639 ideal, whereas other common rock forming minerals may present additional challenges. For
640 example, the slip systems of quartz are relatively well constrained and quartz slip system
641 analysis is widely applied in studies of crustal deformation (e.g. Law *et al.*, 1990; Lloyd *et*
642 *al.*, 1997; Morales *et al.*, 2014). However, single crystals of quartz exhibit complex yield
643 behaviour, with strength dependent not only on temperature but also strain rate and
644 intragranular water content (Hobbs *et al.*, 1972). Consequently, comprehensive
645 measurements of slip system strength, such as those available for calcite (de Bresser and
646 Spiers, 1997), are not currently available for quartz. As a result of these limitations, although
647 it is possible to calculate Schmid factors for quartz slip systems, it is not yet possible to infer
648 which slip systems have sufficient resolved shear stress for slip. Similar detailed

649 considerations must be applied to other common rock-forming minerals.

650 More generally, Schmid factor analysis can require a range of assumptions, depending
651 on the application, which must be critically evaluated. In the present work we are concerned
652 with why dislocation activity ceased at the time that the preserved mylonitic microstructure
653 was formed. In this respect, Schmid factor analysis is highly appropriate because it constrains
654 which slip systems were well aligned for dislocation glide during a hypothetical *future*
655 increment of dislocation-mediated strain. However, a common objective of other rock
656 deformation studies is to interpret how an observed microstructure formed in the first place.
657 Schmid factors calculated for specific points/grains in a mapped microstructure will generally
658 not equal those present during *prior* deformation that lead to formation of the observed
659 microstructure due to microstructural evolution (e.g., grain rotation, grain boundary
660 migration). In some instances, this limitation might be overcome by assuming that the
661 microstructure had ‘on average’ reached a steady state, in combination with analysing
662 Schmid factor distributions over a large portion of the microstructure. However,
663 microstructural steady state, and in particular steady-state CPO, can require shear strains of
664 several hundred percent and can be difficult to prove (Skemer and Hansen, 2016). Averaging
665 over large portions of the microstructure also provides the benefit of reducing the influence of
666 inter- and intra-granular stress heterogeneities. Such heterogeneities have been predicted by
667 numerical modelling (e.g., Pokharel *et al.*, 2014; Lebensohn and Needleman, 2016) and
668 documented in geological crystalline aggregates, including calcite (Quintanilla-Terminel and
669 Evans, 2016) and quartz (Chen *et al.*, 2015), and even in single crystals of olivine (Wallis *et*
670 *al.*, 2017). Therefore, it is important to map Schmid factors over a sufficiently large portion
671 of the microstructure that the averaged internal stress state can be reasonably expected to
672 have approached the macroscopic externally applied stress state during deformation.
673 Notwithstanding these caveats, the present study demonstrates that Schmid factor analysis

674 can provide geologically relevant information, if used in conjunction with appropriate
675 objectives and geological constraints.

676 **6. Conclusions**

677 Schmid factor analysis indicates that calc-mylonites in the Pangong strand of the KFZ
678 deformed primarily by dislocation glide on $r\{10\text{-}14\}\langle\text{-}2021\rangle$ at $\sim 300^\circ\text{C}$ and 98 ± 35 MPa
679 differential stress (Rutter *et al.*, 2007) and by $e\{\text{-}1018\}\langle 40\text{-}41\rangle$ twinning at similar and lower
680 temperatures. In contrast, the critical resolved shear stress for dislocation glide on $f\{\text{-}$
681 $1012\}\langle 2\text{-}201\rangle$ precluded this slip system from activating in the majority of grains under the
682 same conditions. Deformation within the Karakoram Fault Zone continued as the rocks
683 cooled during exhumation, resulting in hardening of the calc-mylonites and thereby leading
684 to a transition from crystal plastic to frictional deformation mechanisms (Rutter *et al.*, 2007,
685 Wallis *et al.*, 2013). One mechanism for such hardening is by the direct temperature effect of
686 increasing critical resolved shear stresses of the active slip and twin systems (De Bresser and
687 Spiers, 1997). However, Schmid factor analysis indicates that this alone was insufficient to
688 induce frictional failure as a greater fraction of the microstructure apparently had sufficient
689 resolved shear stress for dislocation glide at 200°C than at 300°C . Instead, microstructural
690 observations, such as widespread low angle crystallographic misorientations, which increase
691 towards grain boundaries, indicate that intracrystalline strain recovery was inefficient. Strain
692 hardening, due to decreasing efficiency of recovery as temperature decreased, provides an
693 additional hardening mechanism, which we interpret as having led to the onset of frictional
694 and potentially seismogenic deformation in the rocks at this structural level. These findings
695 highlight the importance of detailed understanding of the interplay of strain hardening and
696 recovery processes for models of crystal plasticity, particularly at relatively low homologous
697 temperatures where they impact the transition to frictional and potentially seismogenic
698 deformation.

699 **Acknowledgements**

700 We thank Richard Phillips and Ernie Rutter for providing the sample for this study,
701 Cees Passchier for his editorial handling of the manuscript, and Hans de Bresser and
702 Elisabetta Mariani for their reviews. We are grateful to Rick Law, Gordon Lister and Andrew
703 Turner for helpful discussions. David Wallis and Lars Hansen acknowledge support from the
704 Natural Environment Research Council grant NE/M000966/1. Data reported in this study are
705 available on request from the corresponding author.

706 **References**

- 707 Bachmann, F., Hielscher, R., Schaeben, H., 2010. Texture Analysis with MTEX – Free and
708 Open Source Software Toolbox. *Solid State Phenomena*, 160, 63–68, doi:
709 10.4028/www.scientific.net/SSP.160.63.
- 710 Bestmann, M., Prior, D.J., 2003. Intragranular dynamic recrystallisation in naturally
711 deformed calcite marble: diffusion accommodated grain boundary sliding as a result
712 of subgrain rotation recrystallisation. *Journal of Structural Geology*, 25, 1597–1613,
713 doi: 10.1016/S0191-8141(03)00006-3.
- 714 Bestmann, M., Prior, D.J., Grasemann, B., 2006. Characterisation of deformation and flow
715 mechanics around porphyroclasts in a calcite marble ultramylonite by means of EBSD
716 analysis. *Tectonophysics* 413, 185–200, doi: 10.1016/j.tecto.2005.10.044.
- 717 Boutonnet, E., Leloup, P.H., Arnaud, N., Paquette, J.-L., Davis, W.J., Hattori, K., 2012.
718 Synkinematic magmatism, heterogeneous deformation, and progressive strain
719 localisation in a strike-slip shear zone: The case of the right-lateral Karakorum fault.
720 *Tectonics* 31, TC4012, doi: 10.1029/2011TC003049.
- 721 Brown, E.T., Bendick, R., Bourlès, D.L., Gaur, V., Molnar, P., Raisbeck, G.M., Yiou, F,

- 722 2002. Slip rates of the Karakorum fault, Ladakh, India, determined using cosmogenic
723 ray exposure dating of debris flows and moraines. *Journal of Geophysical Research*
724 107, B9, 2192, doi: 10.1029/2000JB00100.
- 725 Bunge, H., 1982. *Texture Analysis in Materials Science: Mathematical Models*. Butterworths,
726 London, pp. 614.
- 727 Burkhard, M., 1993. Calcite twins, their geometry, appearance and significance as stress-
728 strain markers and indicators of tectonic regime: a review. *Journal of Structural*
729 *Geology* 15, 351–368, doi: 10.1016/0191-8141(93)90132-T.
- 730 Chen, K., Kunz, M., Tamura, N., Wenk, H.-R., 2015. Residual stress preserved in quartz
731 from the San Andreas Fault Observatory at Depth. *Geology* 43, 219–222, doi:
732 10.1130/G36443.
- 733 Covey-Crump, S.J., Rutter, E.H., 1989. Thermally induced grain growth of calcite marbles on
734 Naxos Island, Greece. *Contributions to Mineralogy and Petrology* 101, 69–86, doi:
735 10.1007/BF00387202.
- 736 Cowie, P.A., Phillips, R.J., Roberts, G.P., McCaffrey, K., Zijerveld, L.J.J., Gregory, L.C.,
737 Faure Walker, J., Wedmore, L.N.J., Dunai, T.J., Binnie, S.A., Freeman, S.P.H.T.,
738 Wilcken, K., Shanks, R.P., Huismans, R.S., Papanikolaou, I., Michetti, A.M.,
739 Wilkinson, M., 2017. Orogen-scale uplift in the central Italian Apennines drives
740 episodic behaviour of earthquake faults. *Scientific Reports* 7, 44858, doi:
741 10.1038/srep44858.
- 742 De Bresser, J.H.P., Spiers, C.J., 1990. High temperature deformation of calcite single crystals
743 by r^+ and f^+ slip. In: Knipe, R.J., Rutter, E.H. (Eds.) *Deformation Mechanisms,*
744 *Rheology and Tectonics*. Geological Society, London, Special Publications 54, 285–
745 298, doi: 10.1144/GSL.SP.1990.054.01.25.

- 746 De Bresser, J.H.P., Spiers, C.J., 1993. Slip systems in calcite single crystals deformed at 300–
747 800°C. *Journal of Geophysical Research* 98, 6397–6409, doi: 10.1029/92JB02044.
- 748 De Bresser, J.H.P., Spiers, C.J., 1997. Strength characteristics of the *r*, *f*, and *c* slip systems in
749 calcite. *Tectonophysics* 272, 1–23, doi: 10.1016/S0040-1951(96)00273-9.
- 750 Farla, R.J.M., Fitz Gerald, J.D., Kokkonen, H., Halfpenny, A., Faul, U.H., Jackson, I., 2011.
751 Slip system and EBSD analysis on compressively deformed fine-grained
752 polycrystalline olivine. In: Prior, D.J., Rutter, E.H., Tatham, D.J. (Eds.) *Deformation
753 Mechanisms, Rheology and Tectonics: Microstructures, Mechanics and Anisotropy*.
754 Geological Society, London, Special Publications 360, 225–235, doi:
755 10.1144/SP360.13.
- 756 Fleck, N.A., Muller, G.M., Ashby, M.F., Hutchinson, J.W., 1994. Strain gradient plasticity:
757 theory and experiment. *Acta Metallurgica et Materialia* 42, 475–487, doi:
758 10.1016/0956-7151(94)90502-9.
- 759 Han, R., Hirose, T., Shimamoto, T., 2010. Strong velocity weakening and powder lubrication
760 of simulated carbonate faults at seismic slip rates. *Journal of Geophysical Research*
761 115, B03412.
- 762 Handy, M.R., Hirth, G., Bürgmann, R., 2007. Continental fault structure and rheology from
763 the frictional-viscous transition downward. In: Handy, M.R., Hirth, G., Hovius, N.
764 (Eds.) *Tectonic Faults – Agents of Change on a Dynamic Earth*. The MIT Press,
765 Cambridge, Massachusetts, Dahlem Workshop Report 95, 139–181.
- 766 Hansen, L.N., Zimmerman, M.E., Kohlstedt, D.L., 2011. Grain boundary sliding in San
767 Carlos olivine: Flow law parameters and crystallographic-preferred orientation.
768 *Journal of Geophysical Research* 116, B08201, doi: 10.1029/2011JB008220.

- 769 Hobbs, B.E., McLaren, A.C., Paterson, M.S., 1972. Plasticity of Single Crystals of Synthetic
770 Quartz. In: Heard, H.C., Borg, I.Y., Carter, N.L., Rayleigh, C.B. (Eds.) Flow and
771 Fracture of Rocks. American Geophysical Union, Washington D.C., p. 29–53, doi:
772 10.1029/GM016p0029.
- 773 Ikari, M.J., Marone, C., Saffer, D.M., 2011. On the relation between fault strength and
774 frictional stability. *Geology* 39, 83–86, doi: 10.1130/G31416.1.
- 775 Kennedy, L.A., White, J.C., 2001. Low-temperature recrystallisation in calcite: Mechanisms
776 and consequences. *Geology* 29, 1027–1030, doi: 10.1130/0091-
777 7613(2001)029<1027:LTRICM>2.0.CO;2.
- 778 Law, R.D., Schmid, S.M., Wheeler, J., 1990. Simple shear deformation and quartz
779 crystallographic fabrics: a possible natural example from the Torridon area of NW
780 Scotland. *Journal of Structural Geology* 12, 29–45.
- 781 Lebensohn, R.A., Needleman, A., 2016. Numerical implementation of non-local polycrystal
782 plasticity using fast Fourier transforms. *Journal of the Mechanics and Physics of*
783 *Solids* 97, 333–351, doi: 10.1016/j.jmps. 2016.03.023.
- 784 Liu, M., Evans, B., 1997. Dislocation recovery kinetics in single-crystal calcite. *Journal of*
785 *Geophysical Research* 102, 24801–24809, doi: 10.1029/97JB01892.
- 786 Lloyd, G.E., Farmer, A.B., Mainprice, D., 1997. Misorientation analysis and the formation
787 and orientation of subgrain and grain boundaries. *Tectonophysics* 279, 55–78, doi:
788 10.1016/S0040-1951(97)00115-7.
- 789 Mainprice, D., Bachmann, F., Hielscher, R., Schaeben, H., 2011. Calculating anisotropic
790 physical properties from texture data using the MTEX open source package. In: Prior,
791 D.J., Rutter, E.H., Tatham, D.J. (Eds.) *Deformation Mechanisms, Rheology and*

- 792 Tectonics: Microstructures, Mechanics and Anisotropy. Geological Society, London,
793 Special Publications 360, 175–192, doi: 10.1144/SP360.10.
- 794 Michels, Z.D., Kruckenburg, S.C., Davis, J.R., Tikoff, B., 2015. Determining vorticity axes
795 from grain-scale dispersion of crystallographic orientations. *Geology* 43, 803–806.
- 796 Morales, L.F.G., Lloyd, G.E., Mainprice, D., 2014. Fabric transitions in quartz via
797 viscoplastic self-consistent modeling part I: Axial compression and simple shear
798 under constant strain. *Tectonophysics* 636, 52–69.
- 799 Parsons, A.J., Law, R.D., Lloyd, G.E., Phillips, R.J., Searle, M.P., 2016. Thermo-kinematic
800 evolution of the Annapurna-Dhaulagiri Himalaya, central Nepal: The Composite
801 Orogenic System. *Geochemistry, Geophysics, Geosystems* 17, 1511–1539, doi:
802 10.1002/2015GC006184.
- 803 Phillips, R.J., Parrish, R.R., Searle, M.P., 2004. Age constraints on ductile deformation and
804 long-term slip rates along the Karakoram fault zone, Ladakh. *Earth and Planetary
805 Science Letters* 226, 305–319, doi: 10.1016/j.epsl.2004.07.037.
- 806 Phillips, R.J., Searle, M.P., 2007. Macrostructural and microstructural architecture of the
807 Karakoram fault: Relationship between magmatism and strike–slip faulting. *Tectonics*
808 26, TC3017, doi: 10.1029/2006TC001946.
- 809 Pokharel, R., Lind, J., Kanjarla, A.K., Lebensohn, R.A., Li, S.F., Kenesei, P., Suter, R.M.,
810 Rollett, A.D., 2014. Polycrystal Plasticity: Comparison Between Grain-Scale
811 Observations of Deformation and Simulations. *Annual Review of Condensed Matter
812 Physics* 5, 317–346, doi: 10.1146/annurev-conmatphys-031113-133846.
- 813 Prior, D.J., 1999. Problems in determining the misorientation axes, for small angular
814 misorientations, using electron backscatter diffraction in the SEM. *Journal of*

- 815 Microscopy 195, 217–225, doi: 10.1046/j.1365-2818.1999.00572.x.
- 816 Prior, D.J., Boyle, A.P., Brenker, F., Cheadle, M.C., Day, A., Lopez, G., Peruzzo, L., Potts,
817 G.J., Reddy, S., Spiess, R., Timms, N.E., Trimby, P., Wheeler, J., Zetterström, L.,
818 1999. The application of electron backscatter diffraction and orientation contrast
819 imaging in the SEM to textural problems in rocks. *American Mineralogist* 84, 1741–
820 1759, doi: 10.2138/am-1999-11-1204.
- 821 Prior, D.J., Mariani, E., Wheeler, J., 2009. EBSD in the Earth Sciences: Applications,
822 Common Practice, and Challenges. In: Schwartz, A., Kumar, M., Adams, B., Field, D.
823 (Eds.) *Electron Backscatter Diffraction in Materials Science*. Springer, Boston, MA,
824 345–360, doi: 10.1007/978-0-387-88136-2_26.
- 825 Quintanilla-Terminel, A., Evans, B., 2016. Heterogeneity of inelastic strain during creep of
826 Carrara marble: Microscale strain measurement technique. *Journal of Geophysical*
827 *Research: Solid Earth* 121, 5736–5760, doi: 10.1002/2016JB012970.
- 828 Ralser, S., Hobbs, B.E., Ord, A., 1991. Experimental deformation of a quartz mylonite.
829 *Journal of Structural Geology* 13, 837–850, doi: 10.1016/0191-8141(91)90008-7.
- 830 Renner, J., Evans, B., Siddiqi, G., 2002. Dislocation creep of calcite. *Journal of Geophysical*
831 *Research* 107, B12, 2364, doi: 10.1029/2001JB001680.
- 832 Rowe, K.J., Rutter, E.H., 1990. Palaeostress estimation using calcite twinning: experimental
833 calibration and application to nature. *Journal of Structural Geology* 12, 1–17,
834 10.1016/0191-8141(90)90044-Y.
- 835 Rutter, E.H., 1974. The influence of temperature, strain rate and interstitial water in the
836 experimental deformation of calcite rocks. *Tectonophysics*, 22, 311–334, doi:
837 10.1016/0040-1951(74)90089-4.

- 838 Rutter, E.H., 1995. Experimental study of the influence of stress, temperature and strain on
839 the dynamic recrystallisation of Carrara marble. *Journal of Geophysical Research* 100,
840 24651–24663, doi: 10.1029/95JB02500.
- 841 Rutter, E.H., Faulkner, D.R., Brodie, K.H., Phillips, R.J., Searle, M.P., 2007. Rock
842 deformation processes in the Karakoram fault zone, Ladakh, NW India. *Journal of*
843 *Structural Geology* 29, 1315–1326, doi: 10.1016/j.jsg.2007.05.001.
- 844 Schmid, E., 1928. Zn normal stress law. *Proceedings of the International Congress on*
845 *Applied Mechanics*, Delft, 1924, P. 342.
- 846 Schmid, E., Boas, I.W., 1950. *Plasticity of Crystals*. Chapman and Hall, London, pp. 353.
- 847 Scholz, C.H., 1988. The brittle-plastic transition and the depth of seismic faulting.
848 *Geologische Rundschau* 77, 319–328, doi: 10.1007/BF01848693.
- 849 Skemer, P., Hansen, L.N., 2016. Inferring upper-mantle flow from seismic anisotropy: An
850 experimental perspective. *Tectonophysics* 668–669, 1–14, doi:
851 10.1016/j.tecto.2015.12.003.
- 852 Smith, S.A.F., Billi, A., Di Toro, G., Spiess, R., 2011. Principle Slip Zones in Limestone:
853 Microstructural Characterization and Implications for the Seismic Cycle (Tre Monti
854 Fault, Central Apennines, Italy). *Pure and Applied Geophysics* 168, 2365–2393, doi:
855 10.1007/s00024-011-0267-5.
- 856 Streule, M.J., Phillips, R.J., Searle, M.P., Waters, D.J., Horstwood, M.S.A., 2009. Evolution
857 and chronology of the Pangong Metamorphic Complex adjacent to the Karakoram
858 Fault, Ladakh: constraints from thermobarometry, metamorphic modelling and U Pb
859 geochronology. *Journal of the Geological Society* 166, 919–932, doi: 10.1144/0016-
860 76492008-117.

- 861 Toy, V.G., Prior, D.J., Norris, R.J., 2008. Quartz fabrics in the Alpine Fault mylonites:
862 Influence of pre-existing preferred orientations on fabric development during
863 progressive uplift. *Journal of Structural Geology* 30, 602–621, doi:
864 10.1016/j.jsg.2008.01.001.
- 865 Turner, F.J., 1953. Nature and dynamic interpretation of deformation lamellae in calcite of
866 three marbles. *American Journal of Science* 251, 276–298, doi:
867 10.2475/ajs.251.4.276.
- 868 Van Buer, N.J., Jagoutz, O., Upadhyay, R., Guillong, M., 2015. Mid-crustal detachment
869 beneath western Tibet exhumed where conjugate Karakoram and Longmu-Gozha Co
870 faults intersect. *Earth and Planetary Science Letters* 413, 144–157, doi:
871 10.1016/j.epsl.2014.12.053.
- 872 Verberne, B.A., Niemeijer, A.R., De Bresser, J.H.P., Spiers, C.J., 2015. Mechanical behavior
873 and microstructure of simulated calcite fault gouge sheared at 20–600°C: Implications
874 for natural faults in limestones. *Journal of Geophysical Research: Solid Earth* 120,
875 8169–8196, doi: 10.1002/2015JB012292.
- 876 Wallis D., Hansen, L.N., Britton, T.B., Wilkinson, A.J., 2016a. Geometrically necessary
877 dislocations in olivine obtained using high-angular resolution electron backscatter
878 diffraction. *Ultramicroscopy* 168, 34–45, doi: 10.1016/j.ultramic.2016.06.002.
- 879 Wallis D., Hansen, L.N., Britton, T.B., Wilkinson, A.J., 2017. Dislocation interactions in
880 olivine revealed by HR-EBSD. *Journal of Geophysical Research: Solid Earth*, doi:
881 10.1002/2017JB014513.
- 882 Wallis, D., Phillips, R.J., Lloyd, G.E., 2013. Fault weakening across the frictional-viscous
883 transition zone, Karakoram Fault Zone, NW Himalaya. *Tectonics* 32, 1227–1246, doi:
884 10.1002/tect.20076.

- 885 Wallis, D., Phillips, R.J., Lloyd, G.E., 2014. Evolution of the Eastern Karakoram
886 Metamorphic Complex, Ladakh, NW India, and its relationship to magmatism and
887 regional tectonics. *Tectonophysics* 626, 41–52, doi: 10.1016/j.tecto.2014.03.023.
- 888 Wallis, D., Lloyd, G.E., Phillips, R.J., Parsons, A.J., Walshaw, R.D., 2015. Low effective
889 fault strength due to frictional-viscous flow in phyllonites, Karakoram Fault Zone,
890 NW India. *Journal of Structural Geology* 77, 45–61, doi: 10.1016/j.jsg.2015.05.010.
- 891 Wallis, D., Carter, A., Phillips, R.J., Parsons, A.J., Searle, M.P., 2016b. Spatial variation in
892 exhumation rates across Ladakh and the Karakoram: new apatite fission track data
893 from the Eastern Karakoram, NW India. *Tectonics* 35, doi: 10.1002/2015TC003943.
- 894 Wang, Z.-C., Bai, Q., Dresen, G., Wirth, R., Evans, B., 1996. High-temperature deformation
895 of calcite single crystals. *Journal of Geophysical Research* 101, 20377–20390, doi:
896 10.1029/96JB01186.
- 897 Wenk, H.-R., Takeshita, T., Bechler, E., Erskine, B.G., Matthies, S., 1987. Pure shear and
898 simple shear calcite textures. Comparison of experimental, theoretical and natural
899 data. *Journal of Structural Geology* 9, 731–745, doi: 10.1016/0191-8141(87)90156-8.
- 900 Wheeler, J., Mariani, E., Piazzolo, S., Prior, D.J., Trimby, P., Drury, M.R., 2009. The
901 weighted Burgers vector: a new quantity for constraining dislocation densities and
902 types using electron backscatter diffraction on 2D sections through crystalline
903 materials. *Journal of Microscopy* 233, 482–494, doi: 10.1111/j.1365-
904 2818.2009.03136.x.

Highlights

- Karakoram Fault Zone marbles record transition from dislocation creep to cataclasis
- Novel Schmid factor analysis constrains calcite slip system activity and hardening
- Work hardening caused the transition from dislocation creep to frictional failure
- Depth limit of earthquakes in carbonate faults may be strain-dependent